

Control of Powered Ankle-Foot Prostheses on Compliant Terrain: A Quantitative Approach to Stability Enhancement

Chrysostomos Karakasis, *Graduate Student Member, IEEE*, Camryn Scully, Robert Salati, Panagiotis Artemiadis, *Senior Member, IEEE*

Abstract—Walking on compliant terrain presents a substantial challenge for individuals with lower-limb amputation, further elevating their already high risk of falling. While powered ankle-foot prostheses have demonstrated adaptability across speeds and rigid terrains, control strategies optimized for soft or compliant surfaces remain underexplored. This work experimentally validates an admittance-based control strategy that dynamically adjusts the quasi-stiffness of powered prostheses to enhance gait stability on compliant ground. Human subject experiments were conducted with three healthy individuals walking on two bilaterally compliant surfaces with ground stiffness values of 63 and 25 $\frac{kN}{m}$, representative of real-world soft environments. Controller performance was quantified using phase portraits and two walking stability metrics, offering a direct assessment of fall risk. Compared to a standard phase-variable controller developed for rigid terrain, the proposed admittance controller consistently improved gait stability across all compliant conditions. These results demonstrate the potential of adaptive, stability-aware prosthesis control to reduce fall risk in real-world environments and advance the robustness of human-prosthesis interaction in rehabilitation robotics.

Index Terms—Legged locomotion, prosthetics, powered prosthesis, rehabilitation robotics, admittance control, quasi-stiffness, compliant terrain, gait stability.

I. INTRODUCTION

PEOPLE with a lower limb amputation face an increased risk of falling both during and after their clinical recovery compared to able-bodied individuals [1, 2]. Compliant terrains are an example of surfaces that are commonly found in everyday environments that have been shown to significantly affect walking stability and the risk of falling [3–5]; others include obstacles, uneven surfaces, reduced visibility, etc. Lower-limb prostheses aim to restore mobility and reduce fall risks, with powered prostheses standing out for their energy contribution and adaptability to various tasks and surfaces [6, 7]. However,

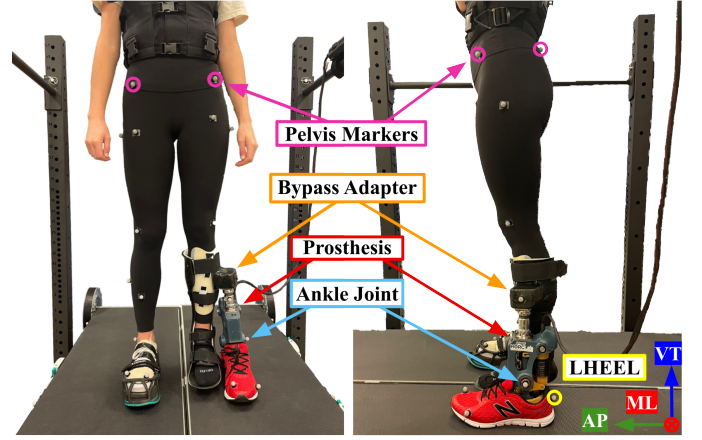


Fig. 1: Front and side view of a subject standing on the Variable Stiffness Treadmill 2 (VST 2), while wearing the powered ankle-foot prosthesis Ruggedized Odyssey Ankle (ROA) attached to ankle bypass adapter. The magenta circles designate the four markers positioned around the pelvis, specifically, the left and right anterior and posterior superior iliac spine. The yellow circle denotes the marker placed on the left heel (LHEEL) of the prosthetic foot. The red, green, and blue axes correspond to the medial-lateral (ML), anterior-posterior (AP), and vertical (VT) directions, respectively.

their robustness across the varied and unpredictable compliant terrains of daily life remains largely untested.

Prior research in bipedal locomotion indicates that modifying ankle stiffness may enhance walking stability over compliant surfaces. Initially, humans have been shown to increase leg and ankle stiffness as ground stiffness decreases [8, 9]. Mimicking this behavior, a bio-inspired controller improved the robustness of a human-like bipedal model to unilateral ground-stiffness perturbations by increasing leg stiffness with ground compliance [10, 11]. In addition to stiffness, the torque-angle relationship, or *quasi-stiffness* [12], of the human ankle has been extensively investigated [13, 14], showing a similar increasing trend with ground compliance [15]. Motivated by these findings, we recently showed that increasing the quasi-stiffness of a powered ankle-foot prosthesis improved gait stability during locomotion over a unilaterally compliant terrain [16]. However, the effect of ankle quasi-stiffness on walking stability has yet to be investigated across different subjects and various bilaterally compliant terrains.

Although quasi-passive ankle-foot prostheses can modulate stiffness with minimal weight and power, they lack the ability to increase push-off work or plantarflexion [7, 17, 18]. Powered prostheses address this by generating mechanical power,

*This material is based upon work supported by the National Science Foundation under Grants No. #2020009, #2015786, #2025797, and #2018905. This scientific paper is partially supported by the Onassis Foundation - Scholarship ID: F ZQ029-1/2020-2021.

Chrysostomos Karakasis, Camryn Scully, and Panagiotis Artemiadis are with the Mechanical Engineering Department, at the University of Delaware, Newark, DE 19716, USA. chryskar@udel.edu, cbscully@udel.edu, partem@udel.edu

Robert Salati was with the Mechanical Engineering Department, at the University of Delaware, Newark, DE 19716, USA. He is now with the Mechanical Engineering Department, at the Rice University, Houston, TX 77005, USA. rsalati@rice.edu

*Corresponding author: partem@udel.edu

typically controlled via phase-variable or impedance-based strategies [6]. Phase-variable controllers enable continuous adaptation to gait timing [16, 19–23], while impedance controllers, often combined with finite state machines, are valued for their simplicity and natural interaction [24–31]. However, traditional impedance designs require extensive manual tuning [32], prompting recent work on variable impedance controllers that adjust parameters continuously [22, 28–32]. Despite these advances enabling stability over uneven terrains and varying speeds [22, 23, 26, 30], existing controllers remain untested on compliant surfaces.

A key line of research has explored quasi-stiffness modulation in powered prostheses to maintain biomimetic joint behavior [16, 22, 33–38]. Early controllers imposed stiffness profiles from able-bodied data and used finite state machine (FSM)s to switch between phases, but were limited to level-ground walking [33, 34, 38]. More recent efforts introduced variable impedance controllers that continuously adjusted parameters based on gait phase and terrain incline [22], yet did not assess stability or performance on compliant surfaces. A phase-based admittance controller was recently proposed to improve stability on compliant terrain [16], showing promising results in one subject over unilaterally compliant ground. However, its generalizability across subjects and bilaterally compliant environments remains untested.

While prior work has advanced prosthesis control through quasi-stiffness modulation and phase-based strategies, a critical aspect often underemphasized is gait stability, especially in challenging environments. Gait stability is essential in designing and evaluating lower-limb prosthesis controllers. Traditional assessments focus on trajectory tracking and convergence in phase portraits [22, 39–41], but these do not fully reflect user stability. To address this, metrics such as maximum Lyapunov exponents and margins of stability have been widely used across populations and conditions, including people with lower-limb amputation, and walking on compliant terrains [3, 4, 42–48]. Combining these with phase portraits enables a more comprehensive evaluation of walking stability.

Accurately evaluating gait stability over compliant terrain has been limited by the difficulty of replicating such surfaces in controlled settings. Earlier studies used foam or gym mats with known stiffness [3–5, 8, 9], but these setups lacked fine stiffness control and made large-scale kinematic and kinetic data collection difficult. To overcome this, our lab developed the Variable Stiffness Treadmill (VST), which could adjust vertical ground stiffness during walking [49, 50]. While the original VST enabled key studies [16, 51–55], it was limited to unilaterally compliant conditions. The newly developed VST 2 addresses this by independently controlling the stiffness of both belts, enabling controlled studies of bilaterally¹ compliant terrains [56].

This paper presents the first experimental evaluation of a novel admittance controller for ankle-foot prostheses aimed at enhancing gait stability over bilaterally compliant terrains. Walking experiments were conducted with three healthy sub-

jects on two compliant surfaces, with stiffness values of 63 and $25 \frac{kN}{m}$, representing real-world soft environments. The admittance controller was compared to a standard phase-variable controller designed for rigid ground. The proposed controller improved overall local dynamic stability across the vast majority of conditions. To our knowledge, this is the first study to systematically assess prosthesis control strategies over multiple compliant terrains, addressing a critical gap in real-world prosthetic performance. These findings represent a significant step toward reducing fall risk for individuals with lower-limb amputation navigating soft or unstable surfaces in daily life.

II. METHODS

A. Ruggedized Odyssey Ankle Prosthesis

For this study, the powered Ruggedized Odyssey Ankle (ROA) prosthesis was used (Fig. 1), developed by SpringActive, Inc. The ROA prosthesis is an updated version of the Walk-Run ankle-foot prosthesis, designed for walking and running [57–60]. The ankle consists of a 250 W brushless DC motor, connected in series with a $377 \frac{kN}{m}$ elastic spring, which then leads to a rigid carbon fiber foot. Therefore, elastic energy is stored and released throughout the gait cycle in the spring, while the motor provides any additional required energy. The prosthesis has two encoders connected to the motor and the ankle joint, and an inertial measurement unit (IMU) fixed to the inside casing above the ankle. The encoders measure the prosthesis ankle angle and motor position, and the IMU measures 3D acceleration and 3D angular velocity. The ankle moment applied by the spring about the ankle joint is estimated through a lookup table (LUT) designed by SpringActive, Inc., as a function of the motor position and ankle angle.

B. Tibia Controller

The ROA prosthesis is by default controlled using the tibia controller (TC), a continuous phase-variable controller proposed in [19]. In essence, the TC leverages tibia kinematics to generate a reference motor trajectory, mimicking ankle angle trajectories observed in the gait of healthy non-disabled individuals. A block diagram illustrating the implementation of the TC to the ROA prosthesis is shown in Fig. 2. Initially, the tibia angular velocity $\dot{\theta}_s$ is calculated through the measurements of a gyroscope included in the IMU of the prosthesis. Then, the gait percent and stride length are determined using the phase plane methodology outlined in [19]. By combining the gait percent and stride length, an appropriate reference ankle angle is derived using a gait LUT, which fits a surface function obtained from motion capture data of healthy non-disabled humans. Consequently, the prosthesis kinematics are used to calculate a corresponding motor position x_q , providing a continuous reference motor trajectory across the entire gait cycle.

In parallel, a moment feedback controller outputs another motor command x_m based on the ankle moment M , which is again computed based on the motor position x and the ankle angle q through a LUT (LUT₁):

$$M = LUT_1(x, q). \quad (1)$$

¹Bilaterally compliant terrains describe surfaces where both legs step on compliant ground.

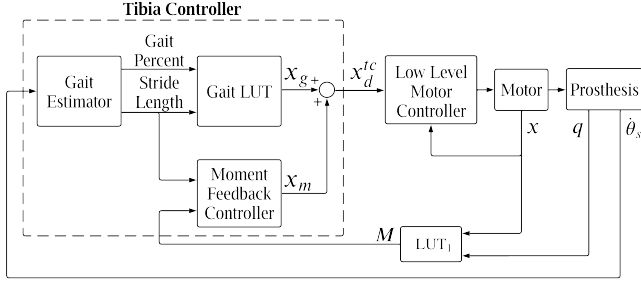


Fig. 2: Block diagram illustrating the implementation of the standard tibia controller (TC) on the lower-limb prosthesis. The tibia angular velocity $\dot{\theta}_s$, determines the gait percent and stride length, subsequently establishing the reference motor position x_g through a gait lookup table (LUT). The ankle moment M is estimated based on the motor position x and the ankle angle q through a LUT (LUT₁). A moment feedback controller exports the motor command x_m based on the ankle moment M to enhance the reference motor command at low stride lengths. The two motor commands are combined to yield the final motor position command x_d^{tc} , sent to the low-level motor controller. The low-level motor controller directs the rotation of the prosthesis ankle joint by issuing precise position commands to the motor.

The moment feedback controller is an additional component to the original TC described in [19], which SpringActive added to amplify the motor command of the TC at low stride lengths. The final motor output x_d^{tc} is a weighted combination of the x_g and x_m commands, which prioritizes the moment feedback controller at low stride lengths ($L_s^n < 1$) by dynamically adjusting each weight:

$$x_d^{tc} = \begin{cases} ax_m + (1-a)x_g, & \text{if } L_s^n < 1, \\ x_g, & \text{else,} \end{cases} \quad (2)$$

$$\text{where, } a = 0.5 \cos(\pi L_s^n) + 0.5, \quad (3)$$

$$L_s^n = \frac{L_s}{SSP}, \quad (4)$$

where L_s is the stride length and L_s^n is the stride length normalized to self-selected pace (SSP); i.e. $L_s^n = 1$ corresponds to SSP. Ultimately, the low-level motor controller, developed by SpringActive, functions as a finely tuned proportional-derivative feedback controller that guarantees accurate motor position tracking across all anticipated speeds and loads associated with the ROA device.

The TC has been successfully used by individuals with transtibial amputation for walking and running on rigid terrain [19,57], and was recently validated for walking over unilaterally compliant surfaces [16]. However, a key limitation of the TC is its inability to adapt the desired ankle trajectory in response to changes in ground compliance. This lack of adaptability can result in unstable gait patterns and increased risk of falls, particularly during abrupt transitions from rigid to soft surfaces – conditions commonly encountered in daily life. This limitation highlights the need for a more robust control approach capable of maintaining stability across varying terrain compliance.

C. Admittance Controller

Inspired by the increase of leg and ankle stiffness observed in humans during locomotion over compliant terrains [8, 9, 15],

the admittance controller (AC) was introduced in [16]. In short, the AC allows the adjustment of the ankle quasi-stiffness in powered prosthetic devices, aiming to assist in walking over compliant terrains. A brief overview of the AC is presented below.

The AC builds upon the TC analyzed in Subsection II-B, extended to permit the modification of ankle quasi-stiffness as required. In general, the AC imposes the following spring-mass-damper behavior on the ankle joint of one degree of freedom:

$$M = K_d(q_d - q_e) + B_d(\dot{q}_d - \dot{q}_e) + I_d(\ddot{q}_d - \ddot{q}_e), \quad (5)$$

where M is the externally applied moment, K_d, B_d, I_d are the stiffness, damping, and inertia of the admittance controller, $q_d, \dot{q}_d, \ddot{q}_d$ are the desired ankle angle and its time derivatives, and $q_e, \dot{q}_e, \ddot{q}_e$ are the equilibrium ankle angle and its time derivatives. As only the control of the ankle quasi-stiffness was of interest in this work, the damping and inertia were set to zero ($B_d = I_d = 0$), yielding the following feedback control law:

$$q_d = q_e + \frac{M}{K_d}. \quad (6)$$

As a consequence, the adjustment of the ankle quasi-stiffness is achieved by specifying a value for the desired stiffness K_d of the admittance controller in (6).

The implementation of the AC to the ROA prosthesis is illustrated in the block diagram of Fig. 3. Initially, the user selects a desired stiffness K_d , and the externally applied moment M is estimated using the ankle moment calculated by the prosthesis (LUT₁), as shown in (1). Subsequently, the function $G = \frac{M}{K_d}$ outputs an ankle angle offset based on the K_d and M . Following (6), this offset is added to the equilibrium ankle angle q_e , resulting in the desired ankle angle q_d . As the equilibrium ankle angle, we used the virtual unloaded reference ankle angle q_u^{tc} , which is calculated through an inverted version of the ankle moment LUT (LUT₂), based on the reference motor position x_d^{tc} of the TC and a virtual zero ankle moment:

$$q_e = q_u^{tc} = \text{LUT}_2(x_d^{tc}, M = 0). \quad (7)$$

This enables the AC to be decoupled from the intrinsic stiffness of the prosthesis, imposed by its dynamics, while inheriting the robust and physiological behavior of the TC. Up to this point, the proposed AC takes a desired stiffness command K_d as input and generates a desired ankle angle q_d to emulate the target quasi-stiffness. Therefore, the AC imposes a desired constant stiffness K_d around an equilibrium angle q_e , derived from an unloaded version of the TC (6).

Next, the desired ankle angle is transformed into a motor position command using a two-component controller (Ankle Controller). First, the dynamics of the prosthesis are fitted in a feedforward (FF) system that uses a LUT (LUT₃) to compute the desired motor position x_{FF} as a function of the desired ankle angle q_d and the measured ankle moment M :

$$x_{FF} = \text{LUT}_3(q_d, M). \quad (8)$$

The LUT₃ was obtained by inverting the LUT created by SpringActive (LUT₁) that approximates the ankle moment M

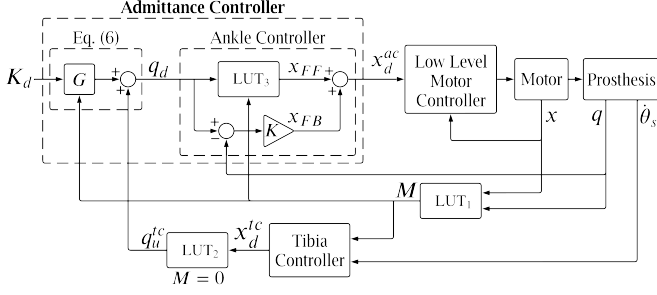


Fig. 3: Block diagram illustrating the implementation of the proposed admittance controller (AC) on the lower-limb prosthesis. The desired stiffness K_d is set, and the admittance controller calculates an ankle angle offset based on the applied moment M . Again, M is derived from a LUT based on the motor position x and the ankle angle q (LUT₁). Simultaneously, the tibia controller calculates a motor position command x_d^{tc} based on the ankle moment and the tibia angular velocity $\dot{\theta}_s$. The virtual unloaded reference ankle angle q_u^{tc} is calculated through an inverted version of the ankle moment LUT (LUT₂), based on x_d^{tc} and a virtual zero ankle moment. The ankle angle offset is added to q_u^{tc} , producing a desired ankle angle q_d , which is then fed into the ankle controller. The ankle controller consists of a feedforward (FF) and a proportional feedback (FB) system, which combined together yield the final motor position command x_d^{ac} sent to the low-level motor controller. The low-level motor controller sends position commands to the motor, causing the rotation of the prosthesis ankle joint.

as a function of the motor position x and the ankle angle q (1). Second, a proportional feedback (FB) controller with a gain $K = 0.45$ produces another motor position command x_{FB} to minimize discrepancies between the desired and actual ankle angles:

$$x_{FB} = K(q_d - q). \quad (9)$$

Then, the feedback and feedforward motor position commands are combined together to yield the desired motor position x_d^{ac} :

$$x_d^{ac} = x_{FF} + x_{FB}. \quad (10)$$

Finally, the desired motor position is forwarded to the low-level motor controller, which ensures precise motor position tracking across conditions, as described for the TC (Subsection II-B).

D. Experimental Protocol

For this study, three healthy non-disabled human subjects (two female and one male, age: 22 ± 1.73 , height: 1.66 ± 0.03 m, weight: 58.98 ± 2.27 kg) completed treadmill walking trials with the ROA prosthesis on a unique instrumented treadmill, the Variable Stiffness Treadmill 2 (VST 2) [56]. Similar to previous studies [16, 27, 60], the prosthesis was attached to the subjects through a carbon fiber ankle bypass adapter fitted around their left shank, without restraining knee movement (see Fig. 1). To address the height difference introduced by the bypass adapter, an adjustable shoe-lift was worn below the right shoe (Evenup Corp., Buford, GA).

The subjects did not have any prior experience with the prosthesis and only performed two visits, one for training and one for experimentation. On the first visit, the subjects first walked on the VST 2 at a self-selected speed without the prosthesis in order to get accustomed to the different stiffness levels of the treadmill. Next, the subjects walked with the prosthesis at a rigid stiffness level for various five-minute

trials, where the treadmill speed was gradually increased until the subjects had identified their comfortable speed. The prosthesis was controlled using the TC for the aforementioned trials. After a comfortable walking speed had been identified, the subjects completed short walking trials at that speed over rigid and bilaterally compliant ground stiffness levels, using both the TC and the AC at three different desired stiffness levels ($K_d = 10, 15$, and 20). The AC K_d values were chosen to align with ankle stiffness values reported in both human and prosthetic studies [9, 14, 15, 61].

On the second visit, the subjects completed eight walking trials at a self-selected walking speed, which all subjects independently chose to be $0.65 \frac{m}{s}$. For the first trial, the subjects walked with the standard TC over a rigid stiffness level for 300 gait cycles. For the next two trials, the subjects walked with the standard TC for 200 gait cycles over two bilaterally compliant terrains of 63 and $25 \frac{kN}{m}$. For the remaining six trials, the prosthesis was controlled using the AC at the following desired stiffness K_d values: 10, 15, and $20 \frac{Nm}{deg}$, over the two bilaterally compliant terrains of 63 and $25 \frac{kN}{m}$. As a reference, these two levels of ground stiffness correspond to surfaces similar to rubber on foam and a foam pad [62]. Subjects were given a five-minute rest between trials to mitigate fatigue. During all trials, a body weight support harness was attached around the torso of the subjects to ensure safety without offloading any weight during normal gait. Additionally, handrails were positioned on the sides of the treadmill for added safety, although they remained unused (Fig. 1). Informed consent was given, and the presented experimental protocol was approved by the University of Delaware Institutional Review Board (IRB ID#: 1520622-8). A supplemental video of all subjects walking across these conditions is accessible for download.

A motion capture system equipped with eight cameras was used to collect kinematic data at 100 Hz (Vicon Motion Systems Ltd.). Specifically, 22 reflective markers were positioned on the lower body of the subjects and their 3D positions were tracked along the Mediolateral (ML), Anteroposterior (AP), and Vertical (VT) directions (Fig. 1). In this study, focus was given only to the markers placed around the pelvis, as well as the heel (LHEEL) of the left prosthetic foot (see Fig. 1). The vertical Ground Reaction Force (GRF) response and the center of pressure (CoP) under each leg of the subjects was recorded at 65 Hz using a force sensor mat (*Medical Sensor 3140TM*, Tekscan, Inc., South Boston, MA) placed underneath both belts of the treadmill. The recorded force mat data were first upsampled from 65 Hz to 100 Hz using linear interpolation to match the frequency rate of the motion capture data, and then were filtered using a moving average filter with a window of 10 samples. Data from the prosthesis, such as ankle angle and moment, were recorded at a rate of 100 Hz. To mitigate any transient artifacts, the first 25 out of the total 200 recorded strides were excluded in all trials.

E. Stability Measures

This section presents the stability metrics used to assess gait and estimate the subjects' risk of falling during the walking

TABLE I: Average Time Delays and Embedding Dimensions

Velocity Type	Time Delay τ (samples)	Embedding Dimension d
ML	10 ± 0.04	3.27 ± 0.45
AP	6.95 ± 0.23	4 ± 0.04
VT	7.39 ± 1.46	4

trials. Similar to previous works [48, 63], the position of the center of mass (CoM) $p_{CoM}(t)$ with respect to time t for each subject was estimated as the mean 3D position of the left and right anterior ($p_{LASI}(t)$ and $p_{RASI}(t)$) and posterior superior ($p_{LPSI}(t)$ and $p_{RPSI}(t)$) iliac spine markers highlighted in Fig. 1:

$$p_{CoM}(t) = \frac{1}{4} \sum_m p_m(t), \quad (11)$$

where $m \in \{LASI, RASI, LPSI, RPSI\}$. The CoM velocity for each subject was computed as the time derivative of the CoM position:

$$\dot{p}_{CoM}(t) = \frac{\Delta p_{CoM}(t)}{\Delta t}, \quad (12)$$

where $\Delta t = 0.01$ s.

1) *Maximum Lyapunov Exponents:* As outlined in [64], the maximum Lyapunov or divergence exponents quantify a system's sensitivity to small perturbations, by tracking the exponential rate of divergence between neighboring trajectories in state space. In particular, larger exponents signify heightened sensitivity to local perturbations, indicating greater divergence and reduced local dynamic stability. Following the approach reported in previous studies, we employed the maximum Lyapunov exponents to evaluate the local dynamic stability of human walking [47].

The maximum Lyapunov exponents were calculated using the algorithm proposed by Rosenstein in [64], following the approach outlined in [65]. First, the estimated 3D CoM position was filtered via a 2^{nd} order, low-pass Butterworth filter (cut-off frequency of 10 Hz), to remove any artifacts unrelated to musculoskeletal motion [66]. Then, the 3D CoM velocity $\dot{p}_{CoM}(t)$ was derived, consisting of a ML, AP, and a VT component (Fig. 1). Following the guidelines reported in [44, 67], the velocity time series were time-normalized to a fixed number of 150 strides and a fixed number of 15000 data points per time series, to obtain accurate estimates of the divergence exponents. From each time-normalized velocity $\dot{p}_\alpha(t_n), \alpha \in \{ML, AP, VT\}$, a high-dimensional attractor $s_\alpha(t_n)$ was recreated through the method of delay embedding [68]:

$$s_\alpha(t_n) = [\dot{p}_\alpha(t_n) \ \dot{p}_\alpha(t_n + \tau_\alpha) \ \dots \ \dot{p}_\alpha(t_n + (d_\alpha - 1)\tau_\alpha)], \quad (13)$$

with τ_α and d_α denoting the time delay and embedding dimensions, respectively. Time delays and embedding dimensions were computed separately for each one of the three velocity types (ML, AP, and VT) using the Average Mutual Information (AMI) algorithm [69], and the False Nearest Neighbor (FNN) algorithm [70], respectively. The average time delays and embedding dimensions across all trials are reported in Table I.

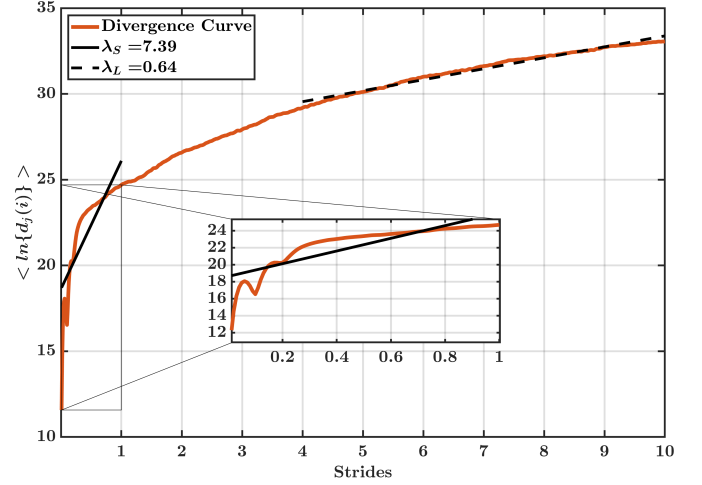


Fig. 4: Representative divergence curve from the ML velocity signal for the trial of the first subject with the tibia controller (TC) over rigid terrain. The orange line represents the divergence curve, while the black solid and dashed lines indicate the least-square fits over the intervals of 0-1 and 4-10 strides, respectively. Divergence exponents λ_S and λ_L represent the slopes of the least-square fits, expressed as $\langle \ln\{d_j(i)\} \rangle$ / stride. Inset: Divergence curve over the interval of 0-1 strides.

For every point within each reconstructed state space $s_\alpha(t_n)$, we identified the nearest neighbor j and tracked the Euclidean distance between them over a 10-stride interval, yielding a time-distance curve $d_j(i)$, with i denoting discrete time instances. The natural logarithmic transformation was applied to all time-distance curves across all neighbor pairs j , and subsequently, an average was computed to obtain the divergence curve, denoted as $\langle \ln\{d_j(i)\} \rangle$. As in previous works, the short-term (λ_S) and long-term (λ_L) Lyapunov exponents were defined as the slopes of linear least-square fits applied to each divergence curve during the intervals of 0-1 strides and 4-10 strides, respectively:

$$\lambda_S = \frac{\langle \ln\{d_j(i_{s1})\} \rangle - \langle \ln\{d_j(i_{s0})\} \rangle}{1 - 0}, \quad (14)$$

$$\lambda_L = \frac{\langle \ln\{d_j(i_{s10})\} \rangle - \langle \ln\{d_j(i_{s4})\} \rangle}{10 - 4}, \quad (15)$$

where $i_{s0}, i_{s1}, i_{s4}, i_{s10}$ denote the time instances corresponding to strides 0, 1, 4, and 10, respectively. The mean duration of strides across all trials was 1.47 ± 0.06 s. To account for variability within each trial, divergence exponents were computed for 25 overlapping windows of 150 strides (175 strides in total) in each trial, and average values along with standard deviations were determined for each exponent [67]. As a representative example, a divergence curve derived from the VT velocity signal for the trial with the tibia controller is illustrated in Fig. 4.

2) *Margins of Stability:* The margins of stability (MOS) have been adopted as a measure of stability, as they depend on the distance between the extrapolated CoM (XcoM) and the base of support (BoS) [45]. The XcoM represents the projected future position of the CoM extrapolated from its velocity, while the BoS signifies the position of either foot during walking. Intuitively, during unstable walking and ultimately falling, the CoM approaches and eventually exceeds the BoS,

showing that greater positive MOS values indicate increased stability. Therefore, the margins of stability, influenced by foot placement, play a crucial role in maintaining stability during walking by ensuring that the feet are positioned laterally and anterior to the XcoM, allowing for effective compensation in response to perturbations and contributing to overall stability [47]. As introduced in [45], the XcoM was defined as

$$\mathbf{XcoM}(t) = \mathbf{p}_{CoM}(t) + \frac{\dot{\mathbf{p}}_{CoM}(t)}{\omega_o}, \quad \omega_o = \sqrt{\frac{g}{l}} \quad (16)$$

where $\mathbf{p}_{CoM}(t)$ and $\dot{\mathbf{p}}_{CoM}(t)$ are the 3D CoM position and velocity, respectively, and ω_o is the eigenfrequency of a hanging non-inverted pendulum of length l , while $g = 9.81 \frac{m}{s^2}$ is the gravity acceleration. Similar to [48], the average Euclidean distance between the CoM and the LHEEL marker was used to calculate the length l , evaluated at foot-strike ($l = 0.97 \pm 0.04 \text{ m}$). The foot-strike events were determined using the real-time kinematic algorithm F-VESPA [71, 72].

The left and right mediolateral margins of stability (MOS_{ML}^L and MOS_{ML}^R) were determined by calculating the minimum medial-lateral distance, within each gait cycle k , between the XcoM and the left and right lateral BoS, defined by the left and right CoP (CoP_{ML}^L and CoP_{ML}^R), respectively [73, 74]:

$$MOS_{ML}^L(k) = \min_i (\|CoP_{ML}^L(i) - \mathbf{XcoM}_{ML}(i)\|), \quad (17)$$

$$MOS_{ML}^R(k) = \min_i (\|CoP_{ML}^R(i) - \mathbf{XcoM}_{ML}(i)\|), \quad (18)$$

with i denoting discrete time instances within each gait cycle. Similarly, the left and right anterior-posterior margins of stability (MOS_{AP}^L and MOS_{AP}^R) were defined by calculating the maximum anterior-posterior distance during each gait cycle k between the XcoM and the left and right anterior BoS, defined by the left and right CoP (CoP_{AP}^L and CoP_{AP}^R), respectively [74]:

$$MOS_{AP}^L(k) = \max_i (\|CoP_{AP}^L(i) - \mathbf{XcoM}_{AP}(i)\|), \quad (19)$$

$$MOS_{AP}^R(k) = \max_i (\|CoP_{AP}^R(i) - \mathbf{XcoM}_{AP}(i)\|), \quad (20)$$

with i again indicating discrete time instances within each gait cycle. Kinematic data were filtered via a 4th order, low-pass Butterworth filter (cut-off frequency of 5 Hz), while the CoP data were filtered using a moving average with a window of 10 samples. A representative example for the calculation of the mediolateral MOS_{ML} (top) and anteroposterior MOS_{AP} (bottom) margins of stability is shown in Fig. 5. Average values and standard deviations were computed for each left and right MOS over a total of 175 steps across all trials.

III. RESULTS

This section involves a comprehensive evaluation of both the admittance and tibia controllers over two bilaterally compliant terrains, in a total of eight walking trials for each of the three subjects. In the first two trials, the tibia controller was tested over two compliant terrains of 63 and 25 $\frac{kN}{m}$. For the last six trials, the admittance controller was tested using the following desired stiffness K_d values: 10, 15, and 20 $\frac{Nm}{deg}$ over the two compliant terrains of 63 and 25 $\frac{kN}{m}$. Initially,

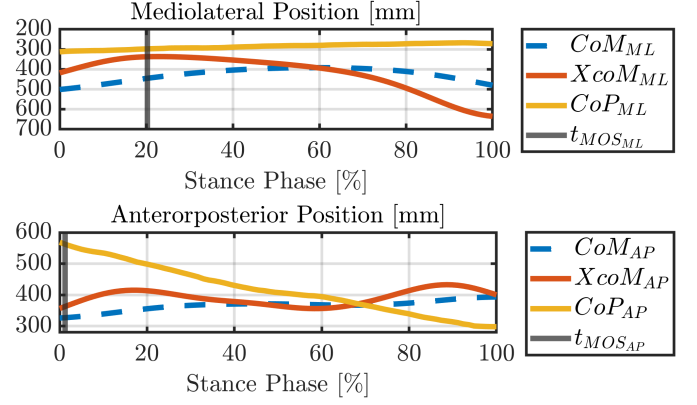


Fig. 5: Representative example for the calculation of the mediolateral MOS_{ML} (top) and anteroposterior MOS_{AP} (bottom) margins of stability for the right side (intact limb) during one gait cycle. Blue dashed lines denote the filtered position of the CoM, while solid orange and yellow lines depict the filtered positions of the XcoM and the CoP, respectively. Vertical solid black lines indicate the timings during the stance phase at which the margins of stability were derived; when the distance between the CoP and the XcoM was minimized in the mediolateral (top) and maximized in the anteroposterior (bottom) direction, respectively. For this example, $MOS_{ML} = 39.21 \text{ mm}$ and $MOS_{AP} = 212.06 \text{ mm}$. For brevity, only the derivation for the right side (intact limb) is shown in this figure, with the left side (prosthetic limb) following a similar procedure.

the performance of the admittance controller in tracking the desired ankle quasi-stiffness is analyzed over the bilaterally compliant terrain. Then, the performance of the two controllers in terms of stability is evaluated using phase portraits and the two proposed stability measures, estimating the probability of falling. All post-processing was implemented and executed in MATLABTM version 9.7 (R2019b) (The MathWorks, Natick, MA USA). Data were statistically tested to determine significance using the Wilcoxon rank-sum test (non-parametric counterpart to the t-test) with an α value of 0.01 [75].

A. Ankle Quasi-stiffness Tracking of Admittance Controller

The performance of the admittance controller in tracking a desired quasi-stiffness was assessed while walking on compliant terrain for three desired stiffness K_d levels: 10, 15 and 20 $\frac{Nm}{deg}$. Following the definition of [12], the ankle quasi-stiffness was represented as the slope of the ankle joint moment-angle curve. Ankle quasi-stiffness was derived throughout the stance phase, defined as the first 60% of the gait cycle starting at foot-strike [76]. The ankle angle and moment of the prosthesis, recorded at 100 Hz, were filtered using a 2nd order, low-pass Butterworth filter (cut-off frequency of 5 Hz). As a representative example, the average moment-angle curves for the third subject during the trials over the first bilaterally compliant terrain of 63 $\frac{kN}{m}$ are depicted in Fig. 6. For each trial, the average moment-angle curve was derived by combining the average profiles of ankle moment and ankle angle across a total of 175 steps. For the sake of comparison, the corresponding average moment-angle curve for the TC was similarly derived, where no control over the ankle quasi-stiffness was imposed. For the same trials, the response of the ankle quasi-stiffness during the stance phase is illustrated in Fig. 7.

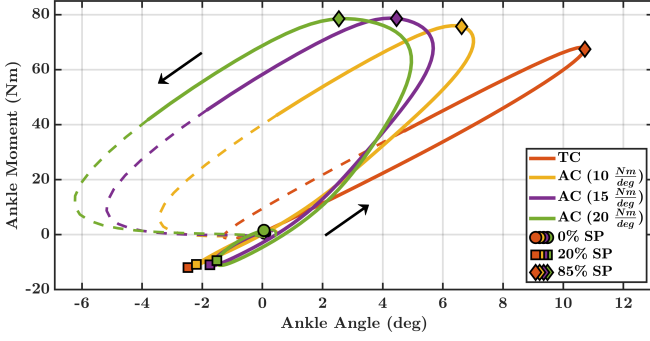


Fig. 6: Moment-angle curves of the powered prosthesis ankle joint for the third subject walking over a bilaterally compliant terrain of $63 \frac{kN}{m}$. The orange lines represent the tibia controller (TC), while the yellow, purple, and green lines correspond to the admittance controller (AC) with desired stiffness values of $K_d = 10, 15$, and $20 \frac{Nm}{deg}$, respectively. Black arrows denote the increasing direction of the gait cycle (GC). Solid and dashed lines signify the stance phase (0-60% GC) and the swing phase (60-100% GC), respectively. Circles (o), squares (□), and diamonds (◇) mark the following time instances during stance phase (SP): foot-strike (0% SP), end of the loading response phase (20% SP), and the beginning of the pre-swing phase (85% SP). Dorsiflexion is indicated by a positive ankle angle.

As depicted in Fig. 6, increasing the desired stiffness of the admittance controller results in a greater instantaneous slope of the moment-angle curve, and hence increased ankle quasi-stiffness. This is further supported by the observation that, when the admittance controller has a higher desired stiffness, there is a reduced angular deflection for the same applied load (moment). Based on these findings, it can be inferred that the ankle joint exhibits notably greater stiffness with all iterations of the admittance controller compared to the tibia controller.

The validity of the aforementioned observations is verified by the response of the ankle quasi-stiffness during the stance phase shown in Fig. 7. In the case of the TC, the prosthesis exhibits a quasi-stiffness that remains consistently near $5 \frac{Nm}{deg}$ throughout the stance phase, even though no specific control was applied to regulate the quasi-stiffness. In comparison to the TC, the AC exhibits significantly higher quasi-stiffness values across the majority of the stance phase, while achieving the desired stiffness levels of $K_d = 10, 15$, and $20 \frac{Nm}{deg}$ around the onset of the terminal stance (60% of the stance phase) [76]. Similarly to previous works, high variability of quasi-stiffness values was observed during the loading response (0-20% of the stance phase) and the pre-swing (85-100% of the stance phase) phases [14]. This behavior is explained by the ankle angle reaching a plateau both before and after the reversal of the ankle moment-angle curve direction, as depicted in Fig. 6. Therefore, we decided to focus only on the response of the quasi-stiffness during the mid and terminal stance phases (20-85% of the stance phase) [76]. In summary, the admittance controller succeeds in significantly increasing the prosthetic ankle's quasi-stiffness, reaching values nearly four times higher than those achieved by the tibia controller.

B. Evaluation of the Tibia and Admittance Controllers

This section involves a comprehensive evaluation of both the admittance and tibia controllers over two bilaterally compliant terrains, in a total of eight walking trials for each of three

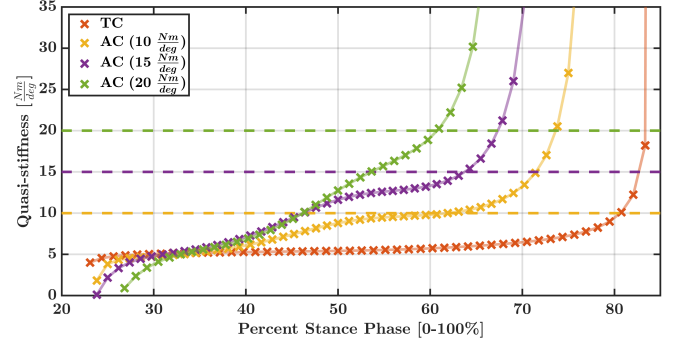


Fig. 7: Ankle quasi-stiffness of the powered prosthesis ankle joint during stance phase for the third subject walking over a bilaterally compliant terrain of $63 \frac{kN}{m}$. The orange line and crosses (x) represent the tibia controller (TC), while the yellow, purple, and green lines and crosses correspond to the admittance controller (AC) with desired stiffness values of $K_d = 10, 15$, and $20 \frac{Nm}{deg}$, respectively. Dashed lines indicate the desired stiffness values of $K_d = 10, 15$, and $20 \frac{Nm}{deg}$. No response is displayed during the loading response phase (0-20% of the stance phase) and the pre-swing phase (85-100% of the stance phase), due to high response variability arising from the reversal of the ankle moment-angle curve direction.

subjects. The evaluation involves analyzing the phase portraits of the prosthetic leg, followed by assessing the maximum Lyapunov exponents and margins of stability, as detailed in Subsection II-E. As a reminder, left and right MOS along the ML and the AP directions were evaluated for each gait cycle for a total of 175 steps across all trials. Then, average values and standard deviations were derived, and data were statistically tested to determine significance. In contrast, the short (λ_S) and long-term (λ_L) maximum Lyapunov exponents were evaluated for 25 overlapping windows of 150 strides for each trial. To facilitate the comparison of the proposed AC relative to the standard TC, the actual change:

$$\Delta\lambda_i = \lambda_i - \lambda_i^{TC}, i \in \{S, L\}, \quad (21)$$

is visualized in subsequent figures for short-term $\Delta\lambda_S$ and long-term $\Delta\lambda_L$ maximum Lyapunov exponents across all controllers for each compliant terrain. As larger $\lambda_{S,L}$ values indicate an increased risk of falling, this suggests that $\Delta\lambda_{S,L} < 0$, $\Delta\lambda_{S,L} \approx 0$, $\Delta\lambda_{S,L} > 0$ indicate improved, similar, and deteriorated local dynamic stability, respectively, when compared to the TC over each compliant terrain. Average values and standard deviations were derived across the 25 windows to show within-trial consistency. The results for both stability measures are also presented in tables as absolute numerical values, along with the average values across subjects.

1) *Phase Portraits:* As a representative example, the phase portraits for the third subject during all four trials over the first bilaterally compliant terrain of $63 \frac{kN}{m}$ are depicted in Fig. 8. It should be noted that similar responses were consistently observed across all three subjects for both bilaterally compliant terrains. For each trial, the phase portrait was derived by combining the profiles of ankle angular velocity and ankle angle across a total of 175 steps. Average phase portraits were also obtained for comparison purposes. The ankle angular velocities were first derived as the time derivatives of the ankle angles recorded at 100 Hz on the prosthesis, and then they were filtered using a 2^{nd} order, low-pass Butterworth filter

Maximum Lyapunov Exponents for Walking Over $63 \frac{kN}{m}$ Compliant Terrain

Controller	Mediolateral (ML) λ_S				Anteroposterior (AP) λ_S				Vertical (VT) λ_S			
	Subject 1	Subject 2	Subject 3	Average	Subject 1	Subject 2	Subject 3	Average	Subject 1	Subject 2	Subject 3	Average
TC	7.13 \pm 0.09	8.46 \pm 0.14	7.93 \pm 0.15	7.84 \pm 0.57	7.27 \pm 0.07	8.64 \pm 0.09	7.07 \pm 0.13	7.66 \pm 0.71	5.65 \pm 0.05	7.31 \pm 0.06	5.66 \pm 0.12	6.21 \pm 0.79
AC (10 $\frac{Nm}{deg}$)	8.30 \pm 0.09	8.82 \pm 0.13	7.49 \pm 0.17	8.20 \pm 0.57	7.32 \pm 0.07	8.24 \pm 0.09	6.77 \pm 0.10	7.44 \pm 0.61	6.04 \pm 0.23	7.29 \pm 0.05	4.82 \pm 0.09	6.05 \pm 1.03
AC (15 $\frac{Nm}{deg}$)	8.07 \pm 0.13	8.13 \pm 0.18	7.84 \pm 0.21	8.01 \pm 0.21	7.21 \pm 0.08	7.73 \pm 0.08	6.70 \pm 0.06	7.21 \pm 0.43	5.42 \pm 0.05	6.54 \pm 0.06	5.12 \pm 0.11	5.69 \pm 0.62
AC (20 $\frac{Nm}{deg}$)	8.13 \pm 0.08	8.74 \pm 0.13	8.46 \pm 0.22	8.44 \pm 0.29	7.04 \pm 0.07	8.30 \pm 0.06	7.10 \pm 0.15	7.48 \pm 0.59	5.54 \pm 0.07	6.89 \pm 0.08	5.07 \pm 0.07	5.83 \pm 0.78

Controller	Mediolateral (ML) λ_L				Anteroposterior (AP) λ_L				Vertical (VT) λ_L			
	Subject 1	Subject 2	Subject 3	Average	Subject 1	Subject 2	Subject 3	Average	Subject 1	Subject 2	Subject 3	Average
TC	0.51 \pm 0.03	0.44 \pm 0.02	0.56 \pm 0.01	0.50 \pm 0.05	0.40 \pm 0.01	0.29 \pm 0.02	0.35 \pm 0.03	0.34 \pm 0.05	0.29 \pm 0.01	0.21 \pm 0.01	0.23 \pm 0.04	0.25 \pm 0.05
AC (10 $\frac{Nm}{deg}$)	0.61 \pm 0.02	0.29 \pm 0.02	0.53 \pm 0.02	0.48 \pm 0.14	0.43 \pm 0.02	0.21 \pm 0.02	0.37 \pm 0.01	0.34 \pm 0.10	0.26 \pm 0.01	0.12 \pm 0.02	0.24 \pm 0.01	0.21 \pm 0.06
AC (15 $\frac{Nm}{deg}$)	0.53 \pm 0.03	0.49 \pm 0.02	0.39 \pm 0.03	0.47 \pm 0.06	0.42 \pm 0.02	0.25 \pm 0.01	0.32 \pm 0.03	0.33 \pm 0.07	0.21 \pm 0.01	0.15 \pm 0.02	0.18 \pm 0.02	0.18 \pm 0.03
AC (20 $\frac{Nm}{deg}$)	0.58 \pm 0.02	0.20 \pm 0.04	0.48 \pm 0.01	0.42 \pm 0.16	0.34 \pm 0.02	0.15 \pm 0.03	0.28 \pm 0.02	0.26 \pm 0.08	0.18 \pm 0.01	0.07 \pm 0.02	0.09 \pm 0.02	0.11 \pm 0.05

TABLE II: Absolute short λ_S (top) and long-term λ_L (bottom) Lyapunov exponents for walking trials over the first bilaterally compliant terrain of $63 \frac{kN}{m}$ stiffness across all subjects. Bold values for the admittance controllers indicate lower values compared to the tibia controller, and hence improved stability. Average columns report the average values across all subjects for each controller.

Margins of Stability in Mediolateral and Anteroposterior Directions Over $63 \frac{kN}{m}$ Compliant Terrain

Controller	Left-Prosthetic MOS _{ML}				Right-Intact MOS _{ML}			
	Subject 1	Subject 2	Subject 3	Average	Subject 1	Subject 2	Subject 3	Average
TC	24.07 \pm 6.46	33.14 \pm 9.31	17.50 \pm 7.24	24.90 \pm 10.06	10.74 \pm 6.21	26.07 \pm 8.64	12.76 \pm 8.17	16.52 \pm 10.30
AC (10 $\frac{Nm}{deg}$)	21.30 \pm 6.62(*)	35.93 \pm 8.65(*)	16.04 \pm 7.42	24.43 \pm 11.34	8.72 \pm 6.42(*)	28.96 \pm 8.01(*)	7.38 \pm 7.79(*)	15.02 \pm 12.36(*)
AC (15 $\frac{Nm}{deg}$)	19.97 \pm 6.62(*)	39.05 \pm 8.32(*)	20.17 \pm 9.11(*)	26.40 \pm 12.05	8.64 \pm 6.00(*)	26.38 \pm 9.26	9.38 \pm 8.39(*)	14.80 \pm 11.45(*)
AC (20 $\frac{Nm}{deg}$)	27.05 \pm 7.59(*)	33.53 \pm 9.15	18.51 \pm 8.06	26.36 \pm 10.31(*)	6.20 \pm 6.09(*)	26.11 \pm 10.50	9.24 \pm 8.53(*)	13.85 \pm 12.24(*)

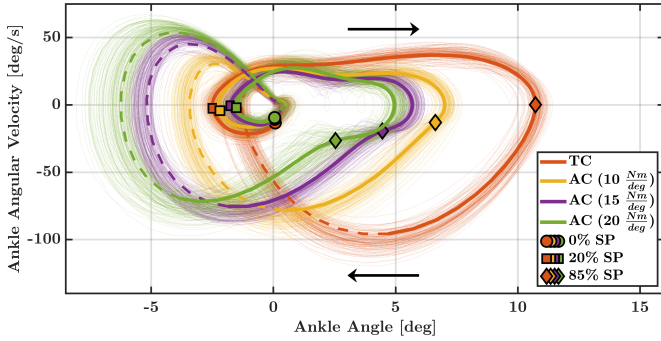


Fig. 8: Phase portraits of the prosthetic leg (ankle angular velocity vs ankle angle) for the third subject walking over a bilaterally compliant terrain of $63 \frac{kN}{m}$. The orange lines represent the tibia controller (TC), while the yellow, purple, and green lines correspond to the admittance controller (AC) with desired stiffness values of $K_d = 10, 15$, and $20 \frac{Nm}{deg}$, respectively. Black arrows point towards the increasing direction of the gait cycle (GC). Opaque lines denote the average phase portraits for each trial, with solid and dashed lines signifying the stance phase (0-60% GC) and the swing phase (60-100% GC), respectively. Semitransparent dotted lines illustrate the phase portraits of all gait cycles for each trial. Circles (\circ), squares (\square), and diamonds (\diamond) mark the time instances of the foot-strike (0% of stance phase), the end of the loading response phase (20% of stance phase), and the beginning of the pre-swing phase (85% of stance phase). Dorsiflexion is indicated by a positive ankle angle.

(cut-off frequency of 5 Hz). These phase portraits show that the prosthesis followed distinct stable periodic orbits for all controllers during the whole duration of the trials, enabling a stable steady-state gait pattern for the user.

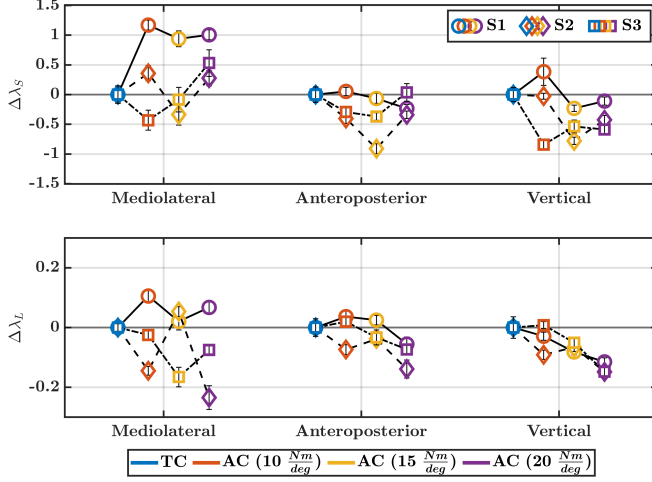
2) *First Bilaterally Compliant Terrain of $63 \frac{kN}{m}$:* The stability evaluation results for the three subjects walking over both rigid and the first bilaterally compliant terrain with a ground stiffness of $63 \frac{kN}{m}$ are depicted in Fig. 9 and Tables II-III. It should be noted that this ground stiffness resulted in a vertical deflection of both legs close to 10 mm.

a) *Short-term Maximum Lyapunov Exponents:* Compared to the TC, the AC overall led to lower ($\Delta\lambda_S < 0$) short-term maximum Lyapunov exponents (λ_S) for all subjects in the AP and VT directions over the $63 \frac{kN}{m}$ compliant terrain (see Fig. 9a and Table II). The association of larger λ_S values with increased probability of falling suggests improved

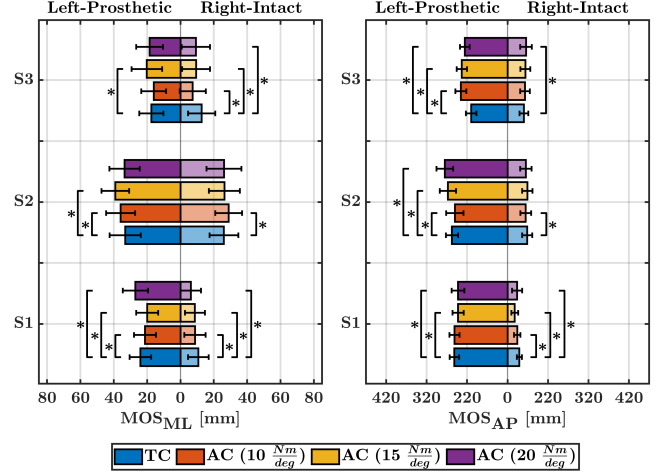
walking stability with the proposed admittance controller in the AP and VT directions. For the ML direction, although the AC of $15 \frac{Nm}{deg}$ led to lower λ_S values for the second and third subjects ($\Delta\lambda_S < 0$), all ACs resulted in greater λ_S values for the first subject ($\Delta\lambda_S > 0$). Average responses across subjects support these findings, showing that the AC improved walking stability in the AP and VT directions, while it deteriorated walking stability in the ML direction (Table II).

b) *Long-term Maximum Lyapunov Exponents:* As depicted in the bottom sections of Fig. 9a and Table II, most versions of the AC achieved lower ($\Delta\lambda_L < 0$) long-term maximum Lyapunov exponents (λ_L) than the TC in all three velocity signals for the second and third subjects over the $63 \frac{kN}{m}$ compliant terrain. As with λ_S , lower λ_L values similarly suggest a reduced probability of falling and hence an improved walking stability. For the first subject, although lower λ_L values are also observed for all three versions of the AC in the VT direction ($\Delta\lambda_L < 0$), greater values are seen for all three ACs in the ML direction ($\Delta\lambda_L > 0$), while only the stiffest AC ($20 \frac{Nm}{deg}$) led to lower values in the AP direction ($\Delta\lambda_L < 0$). Average responses across subjects support these findings, showing that the AC improved walking stability in the AP and VT directions, while it deteriorated walking stability in the ML direction (Table II).

c) *Mediolateral and Anteroposterior MOS:* Figure 9b and Table III show that all versions of the AC achieved either significantly greater or no significantly different MOS_{ML} and MOS_{AP} compared to the TC for the left-prosthetic side of the second and third subject over the $63 \frac{kN}{m}$ compliant terrain. Given that greater MOS values are associated with a lower probability of falling, this indicates that the AC either improved or maintained the walking stability of the two subjects on the prosthesis side in both directions. For the right-intact leg of the second subject, all ACs led to either significantly greater or no significantly different MOS_{ML} and MOS_{AP} compared to the TC in the majority of the cases. For the right side of the third subject, although all ACs led to either significantly greater or no significantly different MOS_{AP} values compared to the TC, significantly lower MOS_{ML} were found



(a) Actual change $\Delta\lambda_i = \lambda_i - \lambda_i^{\text{TC}}$, $i \in \{S, L\}$ in short-term $\Delta\lambda_S$ (top) and long-term $\Delta\lambda_L$ (bottom) maximum Lyapunov exponents between all controllers and the TC over compliant terrain. Positive and negative values indicate a less and more stable behavior than the TC over compliant terrain, respectively.



(b) Mediolateral MOS_{ML} (left) and anteroposterior MOS_{AP} (right) margins of stability for the left-prosthetic and right-intact limb. Higher MOS_{ML} - MOS_{AP} values indicate a more stable behavior.

Fig. 9: Stability measures for walking trials over the first bilaterally compliant terrain of $63 \frac{kN}{m}$ stiffness. Blue and orange markers and bars correspond to the tibia controller (TC) over rigid and compliant terrain, respectively, while yellow, purple, and green markers and bars denote the admittance controller (AC) over compliant terrain with desired stiffness values of 10, 15 and $20 \frac{Nm}{deg}$, respectively. In Fig. 9a, circles (\circ), diamonds (\diamond), and squares (\square) represent the first, second, and third subjects, respectively. Similarly, solid, dashed, and dash-dotted black trendlines correspond to the first, second, and third subjects, respectively. Maximum Lyapunov exponents are expressed as $(\ln\{d_j(i)\})/\text{stride}$. Error bars represent within-trial standard deviations. In Fig. 9b, asterisks (*) indicate significant differences between controllers ($p < 0.01$).

Controller	Left-Prosthetic MOS_{AP}				Right-Intact MOS_{AP}			
	Subject 1	Subject 2	Subject 3	Average	Subject 1	Subject 2	Subject 3	Average
TC	251.43 \pm 11.62	257.33 \pm 15.01	209.67 \pm 13.15	239.47 \pm 25.06	149.22 \pm 6.39	168.51 \pm 12.30	160.39 \pm 10.91	159.37 \pm 12.88
AC (10 $\frac{Nm}{deg}$)	251.05 \pm 12.42	250.16 \pm 21.26(*)	235.16 \pm 13.61(*)	245.46 \pm 17.76	144.10 \pm 7.86(*)	164.97 \pm 13.46(*)	162.98 \pm 11.87	157.35 \pm 14.70
AC (15 $\frac{Nm}{deg}$)	242.11 \pm 13.73(*)	267.21 \pm 20.01(*)	233.02 \pm 12.72(*)	247.45 \pm 21.41(*)	137.87 \pm 8.21(*)	169.02 \pm 12.78	164.07 \pm 12.22	156.99 \pm 17.70
AC (20 $\frac{Nm}{deg}$)	242.19 \pm 15.79(*)	275.09 \pm 20.61(*)	225.59 \pm 12.13(*)	247.62 \pm 26.39(*)	143.63 \pm 12.37(*)	165.23 \pm 14.14	165.75 \pm 14.40(*)	158.20 \pm 17.10

TABLE III: Mediolateral MOS_{ML} (top) and anteroposterior MOS_{AP} (bottom) margins of stability for the left-prosthetic and right-intact limb over the first bilaterally compliant terrain of $63 \frac{kN}{m}$ stiffness across all subjects. Bold values for the admittance controllers indicate greater values compared to the tibia controller, and hence improved stability. Asterisks (*) indicate significant differences between each admittance controller and the tibia controller ($p < 0.01$). Average columns report the average values across all subjects for each controller.

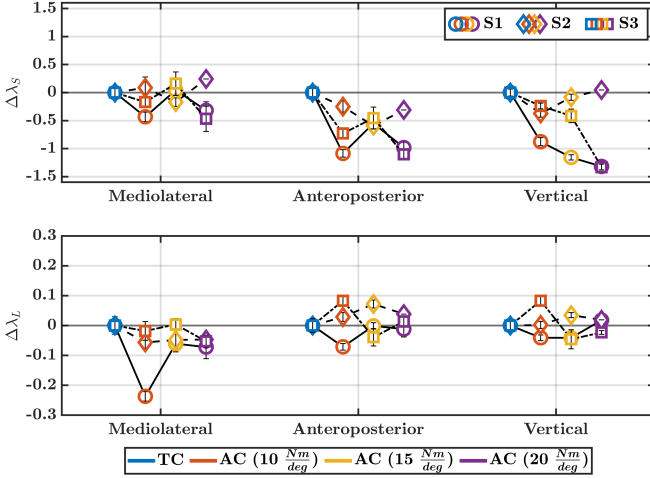
with all versions of the AC. For the first subject, all ACs led to significantly lower MOS_{ML} and MOS_{AP} values for both legs, except for the ACs of 20 and 10 $\frac{Nm}{deg}$ that led to significantly increased MOS_{ML} and non-significant different MOS_{AP} values on the left side, respectively. Average responses across subjects support these findings, showing that the AC improved walking stability in the ML and AP directions for the left-prosthetic side, while it deteriorated walking stability for the right-intact leg (Table II). Finally, it should be noted that a consistent trend of asymmetry was evident across all subjects and controllers, with the margins of stability being greater for the prosthetic (left) leg in comparison to the intact (right) leg.

3) *Second Bilaterally Compliant Terrain of $25 \frac{kN}{m}$:* The stability evaluation results for the three subjects walking over the second bilaterally compliant terrain with a ground stiffness of $25 \frac{kN}{m}$ are depicted in Fig. 10 and Tables IV-V. Subjects experienced significant vertical deflections of both legs close to 20 mm for this ground stiffness.

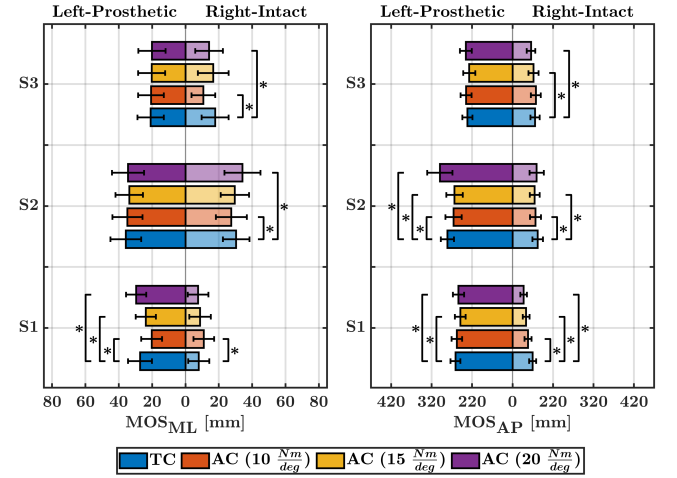
a) *Short-term Maximum Lyapunov Exponents:* The top sections of Fig. 10a and Table IV present that almost all versions of the admittance controller (AC) exhibited lower ($\Delta\lambda_S < 0$) short-term maximum Lyapunov exponents than the tibia controller (TC) over the $25 \frac{kN}{m}$ compliant terrain for all three subjects in all three CoM velocity signals. The

correlation between increased probability of falling and greater λ_S values indicates that the walking stability improved with the proposed admittance controller. The only exceptions to the aforementioned response were found in the ML direction, where greater values ($\Delta\lambda_S > 0$) than the TC over compliant terrain were identified for the second subject with an AC of $20 \frac{Nm}{deg}$ and the third subject with an AC of $15 \frac{Nm}{deg}$. Average responses across subjects support these findings, showing that the AC improved walking stability in all three directions (see Table IV).

b) *Long-term Maximum Lyapunov Exponents:* The bottom sections of Fig. 10a and Table IV demonstrate that all versions of the AC achieved similar or significantly lower ($\Delta\lambda_L < 0$) long-term maximum Lyapunov exponent values than the TC over the $25 \frac{kN}{m}$ compliant terrain in the ML direction for all subjects. Similarly to the relationship seen with λ_L , lower λ_L values imply a reduced probability of falling and hence an improved walking stability with the proposed admittance controller along the ML direction. In the AP and VT directions, a varying behavior was observed across subjects, with the AC leading to lower or similar λ_L for the first subject ($\Delta\lambda_L < 0$), and greater or similar values for the second and third subjects ($\Delta\lambda_L > 0$). Nevertheless, it should be noted that as the desired stiffness of the AC increased, the



(a) Actual change $\Delta\lambda_i = \lambda_i - \lambda_i^{\text{TC}}$, $i \in \{S, L\}$ in short-term $\Delta\lambda_S$ (top) and long-term $\Delta\lambda_L$ (bottom) maximum Lyapunov exponents between all controllers and the TC over compliant terrain. Positive and negative values indicate a less and more stable behavior than the TC over compliant terrain, respectively.



(b) Mediolateral MOS_{ML} (left) and anteroposterior MOS_{AP} (right) margins of stability for the left-prosthetic and right-intact limb. Higher MOS_{ML} - MOS_{AP} values indicate a more stable behavior.

Fig. 10: Stability measures for walking trials over the second bilaterally compliant terrain of $25 \frac{\text{kN}}{\text{m}}$ stiffness. Blue and orange markers and bars correspond to the tibia controller (TC) over rigid and compliant terrain, respectively, while yellow, purple, and green markers and bars denote the admittance controller (AC) over compliant terrain with desired stiffness values of 10, 15 and $20 \frac{\text{Nm}}{\text{deg}}$, respectively. In Fig. 10a, circles (\circ), diamonds (\diamond), and squares (\square) represent the first, second, and third subjects, respectively. Similarly, solid, dashed, and dash-dotted black trendlines correspond to the first, second, and third subjects, respectively. Maximum Lyapunov exponents are expressed as $(\langle \ln\{d_j(i)\} \rangle / \text{stride})$. Error bars represent within-trial standard deviations. In Fig. 10b, asterisks (*) indicate significant differences between controllers ($p < 0.01$).

Maximum Lyapunov Exponents for Walking Over $25 \frac{\text{kN}}{\text{m}}$ Compliant Terrain

Controller	Mediolateral (ML) λ_S				Anteroposterior (AP) λ_S				Vertical (VT) λ_S			
	Subject 1	Subject 2	Subject 3	Average	Subject 1	Subject 2	Subject 3	Average	Subject 1	Subject 2	Subject 3	Average
TC	7.74 ± 0.04	8.74 ± 0.09	8.46 ± 0.10	8.11 ± 0.38	7.83 ± 0.06	8.85 ± 0.11	7.59 ± 0.07	7.74 ± 0.22	6.62 ± 0.04	7.72 ± 0.08	6.17 ± 0.06	6.42 ± 0.30
AC (10 $\frac{\text{Nm}}{\text{deg}}$)	7.31 ± 0.09	8.82 ± 0.19	8.29 ± 0.10	7.81 ± 0.51	6.75 ± 0.07	8.60 ± 0.10	6.86 ± 0.07	6.84 ± 0.29	5.74 ± 0.07	7.35 ± 0.07	5.94 ± 0.05	5.87 ± 0.26
AC (15 $\frac{\text{Nm}}{\text{deg}}$)	7.78 ± 0.14	8.57 ± 0.08	8.62 ± 0.21	8.21 ± 0.46	7.28 ± 0.09	8.26 ± 0.06	7.14 ± 0.19	7.23 ± 0.21	5.46 ± 0.05	7.64 ± 0.05	5.76 ± 0.12	5.65 ± 0.34
AC (20 $\frac{\text{Nm}}{\text{deg}}$)	7.42 ± 0.15	8.98 ± 0	7.99 ± 0.23	7.73 ± 0.39	6.85 ± 0.09	8.54 ± 0	6.49 ± 0.08	6.71 ± 0.33	5.30 ± 0.07	7.77 ± 0	4.85 ± 0.05	5.13 ± 0.44

Controller	Mediolateral (ML) λ_L				Anteroposterior (AP) λ_L				Vertical (VT) λ_L			
	Subject 1	Subject 2	Subject 3	Average	Subject 1	Subject 2	Subject 3	Average	Subject 1	Subject 2	Subject 3	Average
TC	0.60 ± 0.01	0.50 ± 0.03	0.56 ± 0.02	0.58 ± 0.03	0.40 ± 0.02	0.23 ± 0.02	0.31 ± 0.02	0.35 ± 0.05	0.22 ± 0.01	0.11 ± 0.01	0.14 ± 0.01	0.18 ± 0.04
AC (10 $\frac{\text{Nm}}{\text{deg}}$)	0.36 ± 0.02	0.45 ± 0.02	0.54 ± 0.03	0.45 ± 0.09	0.33 ± 0.01	0.26 ± 0.02	0.39 ± 0.02	0.36 ± 0.04	0.18 ± 0.01	0.11 ± 0.01	0.23 ± 0.01	0.20 ± 0.03
AC (15 $\frac{\text{Nm}}{\text{deg}}$)	0.54 ± 0.03	0.46 ± 0.02	0.56 ± 0.02	0.55 ± 0.03	0.40 ± 0.01	0.30 ± 0.01	0.27 ± 0.03	0.33 ± 0.07	0.18 ± 0.01	0.14 ± 0.01	0.10 ± 0.03	0.14 ± 0.05
AC (20 $\frac{\text{Nm}}{\text{deg}}$)	0.53 ± 0.04	0.46 ± 0	0.51 ± 0.02	0.52 ± 0.03	0.39 ± 0.03	0.27 ± 0	0.32 ± 0.02	0.35 ± 0.04	0.24 ± 0.01	0.13 ± 0	0.12 ± 0.01	0.18 ± 0.06

TABLE IV: Absolute short λ_S (top) and long-term λ_L (bottom) Lyapunov exponents for walking trials over the second bilaterally compliant terrain of $25 \frac{\text{kN}}{\text{m}}$ stiffness across all subjects. Bold values for the admittance controllers indicate lower values compared to the tibia controller, and hence improved stability. Average columns report the average values across all subjects for each controller.

Margins of Stability in Mediolateral and Anteroposterior Directions Over $25 \frac{\text{kN}}{\text{m}}$ Compliant Terrain

Controller	Left-Prosthetic MOS_{ML}				Right-Intact MOS_{ML}			
	Subject 1	Subject 2	Subject 3	Average	Subject 1	Subject 2	Subject 3	Average
TC	27.25 ± 7.15	35.78 ± 9.22	20.90 ± 7.94	27.97 ± 10.17	7.93 ± 6.32	30.40 ± 7.98	17.82 ± 8.09	18.72 ± 11.87
AC (10 $\frac{\text{Nm}}{\text{deg}}$)	20.27 ± 6.21(*)	34.80 ± 9.04	20.68 ± 7.75	25.25 ± 10.28(*)	11.04 ± 6.20(*)	27.51 ± 9.29(*)	10.79 ± 7.12(*)	16.45 ± 10.93(*)
AC (15 $\frac{\text{Nm}}{\text{deg}}$)	23.77 ± 6.07(*)	33.71 ± 8.22	20.26 ± 8.12	25.91 ± 9.44(*)	8.79 ± 6.44	29.61 ± 8.52	16.67 ± 9.24	18.35 ± 11.83
AC (20 $\frac{\text{Nm}}{\text{deg}}$)	29.59 ± 6.12(*)	34.47 ± 9.67	20.12 ± 8.15	27.76 ± 9.98	7.56 ± 6.18	34.18 ± 10.79(*)	14.18 ± 8.30(*)	17.92 ± 13.95

Controller	Left-Prosthetic MOS_{AP}				Right-Intact MOS_{AP}			
	Subject 1	Subject 2	Subject 3	Average	Subject 1	Subject 2	Subject 3	Average
TC	261.00 ± 12.07	280.98 ± 16.36	231.54 ± 12.27	257.84 ± 24.50	169.77 ± 8.56	182.09 ± 12.90	175.77 ± 11.49	175.87 ± 12.19
AC (10 $\frac{\text{Nm}}{\text{deg}}$)	257.69 ± 13.10	265.91 ± 20.05(*)	234.89 ± 13.62	252.83 ± 20.60(*)	158.10 ± 8.74(*)	176.63 ± 13.65(*)	177.53 ± 12.19	170.75 ± 14.73(*)
AC (15 $\frac{\text{Nm}}{\text{deg}}$)	249.13 ± 13.40(*)	263.35 ± 20.37(*)	226.94 ± 14.99	246.47 ± 22.29(*)	153.56 ± 8.33(*)	174.64 ± 12.29(*)	171.79 ± 12.56(*)	166.67 ± 14.59(*)
AC (20 $\frac{\text{Nm}}{\text{deg}}$)	253.61 ± 13.70(*)	299.58 ± 31.13(*)	235.08 ± 14.66	261.05 ± 33.71	147.42 ± 8.28(*)	179.57 ± 17.57	165.59 ± 10.65(*)	163.48 ± 18.06(*)

TABLE V: Mediolateral MOS_{ML} (top) and anteroposterior MOS_{AP} (bottom) margins of stability for the left-prosthetic and right-intact limb over the second bilaterally compliant terrain of $25 \frac{\text{kN}}{\text{m}}$ stiffness across all subjects. Bold values for the admittance controllers indicate greater values compared to the tibia controller, and hence improved stability. Asterisks (*) indicate significant differences between each admittance controller and the tibia controller ($p < 0.01$). Average columns report the average values across all subjects for each controller.

AC exhibited similar λ_L values to the TC for all subjects in both directions ($\Delta\lambda_L \approx 0$). Average responses across subjects support these findings, showing that the AC improved walking stability in the ML direction and deteriorated it in the AP and VT directions (Table IV).

c) *Mediolateral and Anteroposterior MOS:* Figure 10b and Table V show no significant difference between the TC and most versions of the AC over the $25 \frac{\text{kN}}{\text{m}}$ compliant terrain in the ML and AP directions for the left-prosthetic side of the second and third subject. Given that larger MOS values

are indicative of a lower probability of falling, this suggests that over this compliant terrain, the AC largely maintained similar walking stability to the TC in both directions for the prosthesis side of the two subjects. The observed pattern was largely consistent, with exceptions noted only for the second subject in the AP direction. On the right-intact side of the second and third subjects, generally all ACs led to either significantly lower or non-significantly different MOS_{ML} and MOS_{AP} compared to the TC, except for the significantly greater MOS_{ML} found for the second subject with the AC of $20 \frac{Nm}{deg}$. For the first subject, significantly lower or non-significantly different margins of stability were identified for most versions of the AC in both directions for both legs. Average responses across subjects indicate that overall the AC deteriorated walking stability in both directions for both sides (Table V). Similarly to the first compliant terrain of $63 \frac{kN}{m}$, the same left-right asymmetry was observed in this compliant terrain as well, with the prosthetic-left leg exhibiting greater margins of stability compared to the right-intact leg.

IV. DISCUSSION

This work presented a novel admittance controller for improving the walking stability of ankle-foot prostheses across various compliant terrains. The proposed controller was evaluated with three healthy non-disabled subjects walking over two bilaterally compliant surfaces with ground stiffness values of 63 and $25 \frac{kN}{m}$. The results of this evaluation were presented in the previous section (III), where the proposed controller was evaluated in terms of tracking a desired quasi-stiffness, as well as in terms of stability and compared to a standard (TC) controller. This section provides a comprehensive summary of the key findings and the significant contributions of this work to the field, while also addressing its limitations and suggesting promising avenues for future investigation.

A. Summary of Main Results

First, the proposed AC was capable of substantially increasing the ankle quasi-stiffness of the prosthesis, achieving approximately four times the stiffness exhibited by the TC (see Section III-A). Specifically, for each desired stiffness value $K_d = 10, 15$, and $20 \frac{Nm}{deg}$, the AC exhibited distinct and continuously increasing quasi-stiffness profiles during the stance phase, while reaching the desired stiffness levels around the onset of the terminal stance (60% of the stance phase) [76].

The performance of the AC was compared to that of the TC in terms of stability, using phase portraits, maximum Lyapunov exponents, and margins of stability. The phase portraits indicated that the prosthesis was able to track distinct stable periodic orbits for all controllers during the whole duration of the eight trials, enabling a stable steady-state gait pattern for all three users over rigid and compliant terrains (see Section III-B1).

For the first bilaterally compliant terrain ($63 \frac{kN}{m}$), the AC improved walking stability in all directions for the second and third subjects, based on both Lyapunov exponents and margins of stability. In contrast, stability for the first subject improved only in the VT direction and declined in the others.

On average, the AC enhanced sagittal-plane stability but reduced mediolateral stability, likely due to its control focus on prosthetic ankle plantar/dorsiflexion.

For the second bilaterally compliant terrain ($25 \frac{kN}{m}$), the AC generally improved or maintained local dynamic stability across all subjects, as indicated by the maximum Lyapunov exponents. Margins of stability showed similar or reduced stability compared to the TC, particularly on the right-intact leg, with the first subject experiencing the most consistent reductions. Despite narrower margins, local stability was not negatively impacted, suggesting the margins remained sufficient. On average, the AC either improved or maintained local dynamic stability, at the expense of narrower margins of stability on both sides. Overall, the AC effectively maintained or improved local dynamic stability for all subjects, even under lower-stiffness conditions.

B. Effect of Ankle Quasi-Stiffness on Gait Stability Across Compliant Terrains

The improved local dynamic stability with the AC compared to the TC highlights the importance of adjusting ankle quasi-stiffness based on ground compliance. On the $63 \frac{kN}{m}$ terrain, stiffer ACs consistently improved stability for the second and third subjects, with Lyapunov exponents showing a trend of increased stability with higher ankle stiffness. A similar pattern was observed on the $25 \frac{kN}{m}$ terrain, primarily in short-term stability, though overall improvements were less pronounced. These findings align with prior work showing that increased ankle or leg stiffness enhances stability in both human and bipedal robot models [10, 11, 16], and are consistent with biomechanics literature indicating that humans increase leg stiffness in response to softer surfaces [9, 15].

C. User Preferences and Perceived Comfort Across Terrain and Controller Conditions

User preference for ankle quasi-stiffness appeared to influence perceived walking stability [61]. After each trial, participants were asked to rate comfort and compare the controllers. During initial training on rigid terrain, all subjects preferred the TC, finding the ACs too spring-like and stiff. However, during longer trials on compliant terrain, subjects 1 and 3 favored the lower-stiffness ACs over the TC, while subject 2 preferred the TC on the stiffer terrain ($63 \frac{kN}{m}$) and the $10 \frac{Nm}{deg}$ AC on the softer terrain ($25 \frac{kN}{m}$). They noted that increased quasi-stiffness, though excessive on firmer ground, enhanced push-off and balance on softer surfaces.

Optimal ankle quasi-stiffness should account for ground stiffness, walking stability, and user comfort. A recent study identified user-preferred stiffness levels for variable-stiffness prostheses and linked these preferences to biomechanical and behavioral factors [61]. Building on this, the same group developed an offline machine learning model that accurately predicts a user's preferred ankle stiffness [77]. In parallel, a pattern-recognition algorithm has been proposed to detect upcoming surface stiffness changes in real time using EMG and kinematic data [78, 79]. Together with the findings of this study, these advances support the development of adaptive

control frameworks that adjust ankle stiffness in real time based on user input, stability needs, and terrain properties.

D. Limitations of the Study and Future Work

The main limitation of this study is that the prosthesis was tested on healthy, non-disabled individuals rather than participants with lower-limb amputation. Specifically, three subjects used a carbon fiber ankle bypass adapter mounted around their left shank to simulate prosthesis use. While this approach does not fully replicate the biomechanics of transtibial amputation, it is a widely accepted and commonly used method in prosthetics research [16, 27, 41, 60]. The bypass adapter effectively isolates the biological ankle joint while preserving natural knee movement, making it a practical and well-established approximation. That said, it introduces some known limitations; most notably a mediolateral offset due to the prosthesis being mounted beside the intact limb (Fig. 1). This offset may influence step width and mediolateral stability, contributing to the left–right asymmetries observed in the margins of stability (Figs. 9–10). Similar asymmetries, however, have also been reported in both healthy individuals and those with transfemoral amputation [48, 73, 80]. Disentangling the effects of the adapter offset from natural gait variability is challenging and beyond the scope of this study. Nonetheless, by analyzing stability metrics separately for each side, we are able to draw meaningful conclusions about side-specific stability improvements across controllers and conditions.

Additionally, limited exposure and training with the prosthesis may have influenced stability outcomes. While all subjects practiced with the device and controllers until comfortable, individuals with lower-limb amputation are likely to be more experienced and better adapted to prosthetic use. For this reason, future work will include testing with individuals with transtibial amputation to further validate the controller’s effectiveness over bilaterally compliant terrains.

While increasing ankle quasi-stiffness improved stability on the first compliant terrain, it did not significantly enhance gait stability on the softer $25 \frac{kN}{m}$ surface, which is the lowest stiffness the VST 2 can achieve [56]. This may indicate that the terrain was too compliant for stiffness changes to have a meaningful effect. Moreover, the tested stiffness range ($10\text{--}20; \frac{Nm}{deg}$) aligns with values reported in both human and prosthetic studies [9, 14, 15, 61], making it unlikely that higher values would offer further benefit. However, other admittance controller parameters – such as damping or equilibrium angle – could also influence stability and warrant further exploration. These could be implemented as constants or time-varying functions, as seen in modern variable impedance controllers [22, 28–32]. While this study focused on isolating the stiffness effect, future work should investigate how tuning these additional parameters affects walking stability over compliant terrain.

While this study introduces a significant advancement in evaluating prosthesis control over compliant terrains, future research can build on this foundation by incorporating additional stability measures. The metrics used here were carefully selected for their relevance and reliability, but other

measures, such as temporal gait symmetry, trunk pitch and roll angles, and angular velocity, have also been shown to effectively capture gait stability and postural control across various perturbation scenarios [5, 47, 81, 82]. Including such metrics in future studies could offer deeper insights into locomotion over compliant surfaces and further inform the development and evaluation of next-generation lower-limb prosthesis controllers.

V. CONCLUSION

This work introduces a novel admittance controller specifically designed to enhance walking stability in ankle-foot prostheses across a range of compliant terrains. Its effectiveness was demonstrated through treadmill experiments with three healthy participants walking over two bilaterally compliant surfaces with stiffness values of 63 and $25 \frac{kN}{m}$. Compared to a standard phase-variable controller optimized for rigid ground, the proposed controller consistently improved local dynamic stability across all subjects and conditions. By addressing the critical challenge of maintaining stability on soft, real-world surfaces, this study marks a significant step toward more robust, adaptable prosthetic control. The findings lay the groundwork for advancing powered prostheses that can better support individuals with lower-limb amputation in navigating everyday environments with greater confidence and safety.

REFERENCES

- [1] N. Steinberg, A. Gottlieb, I. Siev-Ner, and M. Plotnik, “Fall incidence and associated risk factors among people with a lower limb amputation during various stages of recovery—a systematic review,” *Disability and rehabilitation*, vol. 41, no. 15, pp. 1778–1787, 2019.
- [2] M. E. Eveld, S. T. King, K. E. Zelik, and M. Goldfarb, “Factors leading to falls in transfemoral prosthesis users: a case series of sound-side stumble recovery responses,” *Journal of NeuroEngineering and Rehabilitation*, vol. 19, no. 1, p. 101, 2022.
- [3] M. D. Chang, E. Sejdić, V. Wright, and T. Chau, “Measures of dynamic stability: Detecting differences between walking overground and on a compliant surface,” *Human movement science*, vol. 29, no. 6, pp. 977–986, 2010.
- [4] M. J. MacLellan and A. E. Patla, “Adaptations of walking pattern on a compliant surface to regulate dynamic stability,” *Experimental brain research*, vol. 173, pp. 521–530, 2006.
- [5] D. S. Marigold and A. E. Patla, “Adapting locomotion to different surface compliances: Neuromuscular responses and changes in movement dynamics,” *Journal of Neurophysiology*, vol. 94, no. 3, pp. 1733–1750, 2005, PMID: 15888535. [Online]. Available: <https://doi.org/10.1152/jn.00019.2005>
- [6] R. Gehlhar, M. Tucker, A. J. Young, and A. D. Ames, “A review of current state-of-the-art control methods for lower-limb powered prostheses,” *Annual Reviews in Control*, vol. 55, pp. 142–164, 2023. [Online]. Available: <https://www.sciencedirect.com/science/article/pii/S136757882300007X>
- [7] E. M. Glanzner and P. G. Adamczyk, “Design and validation of a semi-active variable stiffness foot prosthesis,” *IEEE Transactions on Neural Systems and Rehabilitation Engineering*, vol. 26, no. 12, pp. 2351–2359, 2018.
- [8] D. P. Ferris, M. Louie, and C. T. Farley, “Running in the real world: adjusting leg stiffness for different surfaces,” *Proceedings of the Royal Society of London. Series B: Biological Sciences*, vol. 265, no. 1400, pp. 989–994, 1998.
- [9] K. Xie, Y. Lyu, X. Zhang, and R. Song, “How compliance of surfaces affects ankle moment and stiffness regulation during walking,” *Frontiers in Bioengineering and Biotechnology*, p. 759, 2021.
- [10] C. Karakasis, I. Poulakakis, and P. Artemiadis, “Robust dynamic walking for a 3d dual-slip model under one-step unilateral stiffness perturbations: Towards bipedal locomotion over compliant terrain,” in *2022 30th Mediterranean Conference on Control and Automation (MED)*. IEEE, 2022, pp. 969–975.

- [11] C. Karakasis, I. Poulakakis, and P. Artemiadis, "An Energy-Based Framework for Robust Dynamic Bipedal Walking Over Compliant Terrain," *Journal of Dynamic Systems, Measurement, and Control*, vol. 146, no. 2, p. 021008, 12 2023. [Online]. Available: <https://doi.org/10.1115/1.4064094>
- [12] E. J. Rouse, R. D. Gregg, L. J. Hargrove, and J. W. Sensinger, "The difference between stiffness and quasi-stiffness in the context of biomechanical modeling," *IEEE Transactions on Biomedical Engineering*, vol. 60, no. 2, pp. 562–568, 2012.
- [13] H. Lee, E. J. Rouse, and H. I. Krebs, "Summary of human ankle mechanical impedance during walking," *IEEE journal of translational engineering in health and medicine*, vol. 4, pp. 1–7, 2016.
- [14] E. J. Rouse, L. J. Hargrove, E. J. Perreault, and T. A. Kuiken, "Estimation of human ankle impedance during the stance phase of walking," *IEEE Transactions on Neural Systems and Rehabilitation Engineering*, vol. 22, no. 4, pp. 870–878, 2014.
- [15] C. T. Farley, H. H. Houdijk, C. Van Strien, and M. Louie, "Mechanism of leg stiffness adjustment for hopping on surfaces of different stiffnesses," *Journal of applied physiology*, vol. 85, no. 3, pp. 1044–1055, 1998.
- [16] C. Karakasis, R. Salati, and P. Artemiadis, "Adjusting the quasi-stiffness of an ankle-foot prosthesis improves walking stability during locomotion over compliant terrain," in *2023 IEEE/RSJ International Conference on Intelligent Robots and Systems (IROS)*, 2023, pp. 2140–2145.
- [17] M. K. Shepherd and E. J. Rouse, "The vspa foot: A quasi-passive ankle-foot prosthesis with continuously variable stiffness," *IEEE Transactions on Neural Systems and Rehabilitation Engineering*, vol. 25, no. 12, pp. 2375–2386, 2017.
- [18] H. L. Bartlett, S. T. King, M. Goldfarb, and B. E. Lawson, "A semi-powered ankle prosthesis and unified controller for level and sloped walking," *IEEE Transactions on Neural Systems and Rehabilitation Engineering*, vol. 29, pp. 320–329, 2021.
- [19] M. A. Holgate, T. G. Sugar, and A. W. Bohler, "A novel control algorithm for wearable robotics using phase plane invariants," in *2009 IEEE International Conference on Robotics and Automation*. IEEE, 2009, pp. 3845–3850.
- [20] T. K. Best, K. R. Embry, E. J. Rouse, and R. D. Gregg, "Phase-variable control of a powered knee-ankle prosthesis over continuously varying speeds and inclines," in *2021 IEEE/RSJ International Conference on Intelligent Robots and Systems (IROS)*. IEEE, 2021, pp. 6182–6189.
- [21] S. Cheng, C. A. Laubscher, and R. D. Gregg, "Controlling powered prosthesis kinematics over continuous transitions between walk and stair ascent," in *2023 IEEE/RSJ International Conference on Intelligent Robots and Systems (IROS)*, 2023, pp. 2108–2115.
- [22] T. K. Best, C. G. Welker, E. J. Rouse, and R. D. Gregg, "Data-driven variable impedance control of a powered knee-ankle prosthesis for adaptive speed and incline walking," *IEEE Transactions on Robotics*, vol. 39, no. 3, pp. 2151–2169, 2023.
- [23] S. Cheng, C. A. Laubscher, and R. D. Gregg, "Controlling powered prosthesis kinematics over continuous inter-leg transitions between walking and stair ascent/descent," *IEEE Transactions on Neural Systems and Rehabilitation Engineering*, vol. 32, pp. 3891–3901, 2024.
- [24] F. Sup, H. A. Varol, J. Mitchell, T. Withrow, and M. Goldfarb, "Design and control of an active electrical knee and ankle prosthesis," in *2008 2nd IEEE RAS & EMBS International Conference on Biomedical Robotics and Biomechanics*, 2008, pp. 523–528.
- [25] A. M. Simon, K. A. Ingraham, N. P. Fey, S. B. Finucane, R. D. Lipschutz, A. J. Young, and L. J. Hargrove, "Configuring a powered knee and ankle prosthesis for transfemoral amputees within five specific ambulation modes," *PLOS ONE*, vol. 9, no. 6, pp. 1–10, 06 2014. [Online]. Available: <https://doi.org/10.1371/journal.pone.0099387>
- [26] L. M. Sullivan, S. Creveling, M. Cowan, L. Gabert, and T. Lenzi, "Powered knee and ankle prosthesis control for adaptive ambulation at variable speeds, inclines, and uneven terrains," in *2023 IEEE/RSJ International Conference on Intelligent Robots and Systems (IROS)*, 2023, pp. 2128–2133.
- [27] R. R. Posh, J. P. Schmiedeler, and P. M. Wensing, "Finite-state impedance and direct myoelectric control for robotic ankle prostheses: Comparing their performance and exploring their combination," *IEEE Transactions on Neural Systems and Rehabilitation Engineering*, vol. 31, pp. 2778–2788, 2023.
- [28] A. Mohammadi and R. D. Gregg, "Variable impedance control of powered knee prostheses using human-inspired algebraic curves," *Journal of Computational and Nonlinear Dynamics*, vol. 14, no. 10, p. 101007, 09 2019. [Online]. Available: <https://doi.org/10.1115/1.4043002>
- [29] N. A. Kumar, W. Hong, and P. Hur, "Impedance control of a transfemoral prosthesis using continuously varying ankle impedances and multiple equilibria," in *2020 IEEE International Conference on Robotics and Automation (ICRA)*, 2020, pp. 1755–1761.
- [30] A. J. Lee, C. A. Laubscher, T. K. Best, and R. D. Gregg, "Towards a unified approach for continuously-variable impedance control of powered prosthetic legs over walking speeds and inclines," in *2024 IEEE International Conference on Robotics and Automation (ICRA)*, 2024, pp. 944–950.
- [31] R. J. Cortino, T. K. Best, and R. D. Gregg, "Data-driven phase-based control of a powered knee-ankle prosthesis for variable-incline stair ascent and descent," *IEEE Transactions on Medical Robotics and Bionics*, vol. 6, no. 1, pp. 175–188, 2024.
- [32] E. Reznick, T. K. Best, and R. Gregg, "A clinical tuning framework for continuous kinematic and impedance control of a powered knee-ankle prosthesis," 2024. [Online]. Available: <https://arxiv.org/abs/2412.10154>
- [33] T. Lenzi, L. Hargrove, and J. W. Sensinger, "Preliminary evaluation of a new control approach to achieve speed adaptation in robotic transfemoral prostheses," in *2014 IEEE/RSJ International Conference on Intelligent Robots and Systems*, 2014, pp. 2049–2054.
- [34] T. Lenzi, L. Hargrove, and J. Sensinger, "Speed-adaptation mechanism: Robotic prostheses can actively regulate joint torque," *IEEE Robotics & Automation Magazine*, vol. 21, no. 4, pp. 94–107, 2014.
- [35] S. Hood, L. Gabert, and T. Lenzi, "Powered knee and ankle prosthesis with adaptive control enables climbing stairs with different stair heights, cadences, and gait patterns," *IEEE Transactions on Robotics*, vol. 38, no. 3, pp. 1430–1441, 2022.
- [36] L. Gabert, S. Hood, M. Tran, M. Cempini, and T. Lenzi, "A compact, lightweight robotic ankle-foot prosthesis: Featuring a powered polycentric design," *IEEE Robotics & Automation Magazine*, vol. 27, no. 1, pp. 87–102, 2020.
- [37] J. Mendez, S. Hood, A. Gunnel, and T. Lenzi, "Powered knee and ankle prosthesis with indirect volitional swing control enables level-ground walking and crossing over obstacles," *Science Robotics*, vol. 5, no. 44, p. eaba6635, 2020. [Online]. Available: <https://www.science.org/doi/abs/10.1126/scirobotics.aba6635>
- [38] T. Elery, S. Rezazadeh, E. Reznick, L. Gray, and R. D. Gregg, "Effects of a powered knee-ankle prosthesis on amputee hip compensations: A case series," *IEEE Transactions on Neural Systems and Rehabilitation Engineering*, vol. 28, no. 12, pp. 2944–2954, 2020.
- [39] D. Quintero, D. J. Villarreal, D. J. Lambert, S. Kapp, and R. D. Gregg, "Continuous-phase control of a powered knee-ankle prosthesis: Amputee experiments across speeds and inclines," *IEEE Transactions on Robotics*, vol. 34, no. 3, pp. 686–701, 2018.
- [40] R. D. Gregg, T. Lenzi, L. J. Hargrove, and J. W. Sensinger, "Virtual constraint control of a powered prosthetic leg: From simulation to experiments with transfemoral amputees," *IEEE Transactions on Robotics*, vol. 30, no. 6, pp. 1455–1471, 2014.
- [41] R. Gehlhar and A. D. Ames, "Emulating human kinematic behavior on lower-limb prostheses via multi-contact models and force-based nonlinear control," in *2023 IEEE International Conference on Robotics and Automation (ICRA)*, 2023, pp. 10 429–10 435.
- [42] D. H. Gates, S. J. Scott, J. M. Wilken, and J. B. Dingwell, "Frontal plane dynamic margins of stability in individuals with and without transtibial amputation walking on a loose rock surface," *Gait & posture*, vol. 38, no. 4, pp. 570–575, 2013.
- [43] F. B. Rodrigues, A. O. Andrade, and M. F. Vieira, "Effects of inclined surfaces on gait variability and stability in unilateral lower limb amputees," *Medical & Biological Engineering & Computing*, vol. 57, pp. 2337–2346, 2019.
- [44] P. C. Raffalt, J. A. Kent, S. R. Wurdeman, and N. Stergiou, "Selection procedures for the largest lyapunov exponent in gait biomechanics," *Annals of biomedical engineering*, vol. 47, pp. 913–923, 2019.
- [45] A. Hof, M. Gazendam, and W. Sinke, "The condition for dynamic stability," *Journal of biomechanics*, vol. 38, no. 1, pp. 1–8, 2005.
- [46] P. M. McAndrew, J. M. Wilken, and J. B. Dingwell, "Dynamic stability of human walking in visually and mechanically destabilizing environments," *Journal of biomechanics*, vol. 44, no. 4, pp. 644–649, 2011.
- [47] S. M. Bruijn, O. Meijer, P. Beek, and J. H. van Dieen, "Assessing the stability of human locomotion: a review of current measures," *Journal of the Royal Society Interface*, vol. 10, no. 83, p. 20120999, 2013.
- [48] P. M. M. Young, J. M. Wilken, and J. B. Dingwell, "Dynamic margins of stability during human walking in destabilizing environments," *Journal of biomechanics*, vol. 45, no. 6, pp. 1053–1059, 2012.
- [49] A. Barkan, J. Skidmore, and P. Artemiadis, "Variable stiffness treadmill (VST): A novel tool for the investigation of gait," in *2014 IEEE International Conference on Robotics and Automation (ICRA)*. IEEE, 2014, pp. 2838–2843.

- [50] J. Skidmore, A. Barkan, and P. Artemiadis, "Variable stiffness treadmill (VST): System development, characterization, and preliminary experiments," *IEEE/ASME Transactions on Mechatronics*, vol. 20, no. 4, pp. 1717–1724, 2014.
- [51] J. Skidmore, A. Barkan, and P. Artemiadis, "Investigation of contralateral leg response to unilateral stiffness perturbations using a novel device," in *2014 IEEE/RSJ International Conference on Intelligent Robots and Systems*. IEEE, 2014, pp. 2081–2086.
- [52] J. Skidmore and P. Artemiadis, "Unilateral floor stiffness perturbations systematically evoke contralateral leg muscle responses: a new approach to robot-assisted gait therapy," *IEEE Transactions on Neural Systems and Rehabilitation Engineering*, vol. 24, no. 4, pp. 467–474, 2015.
- [53] M. Drolet, E. Q. Yumbla, B. Hobbs, and P. Artemiadis, "On the effects of visual anticipation of floor compliance changes on human gait: Towards model-based robot-assisted rehabilitation," in *2020 IEEE International Conference on Robotics and Automation (ICRA)*. IEEE, 2020, pp. 9072–9078.
- [54] V. Chambers and P. Artemiadis, "Repeated robot-assisted unilateral stiffness perturbations result in significant aftereffects relevant to post-stroke gait rehabilitation," in *2022 International Conference on Robotics and Automation (ICRA)*. IEEE, 2022, pp. 5426–5433.
- [55] V. Chambers and P. Artemiadis, "Using robot-assisted stiffness perturbations to evoke aftereffects useful to post-stroke gait rehabilitation," *Frontiers in Robotics and AI*, vol. 9, 2022.
- [56] V. Chambers, B. Hobbs, W. Gaither, A. Zhou, C. Karakasis, and P. Artemiadis, "The variable stiffness treadmill 2: Development and validation of a unique tool to investigate locomotion on compliant terrains," *Journal of Mechanisms and Robotics*, vol. 17, no. 3, 2025.
- [57] J. Ward, K. Schroeder, D. Vehon, R. Holgate, A. Boehler, and M. Grimmer, "A rugged microprocessor controlled ankle-foot prosthesis for running," in *39th annual meeting of the american society of biomechanics (ASB)*. Columbus, 2015.
- [58] M. Grimmer, M. Holgate, J. Ward, A. Boehler, and A. Seyfarth, "Feasibility study of transtibial amputee walking using a powered prosthetic foot," in *2017 International Conference on Rehabilitation Robotics (ICORR)*. IEEE, 2017, pp. 1118–1123.
- [59] A. Naseri, M. Grimmer, A. Seyfarth, and M. A. Sharbafi, "Neuromechanical force-based control of a powered prosthetic foot," *Wearable Technologies*, vol. 1, p. e6, 2020.
- [60] G. Clark and H. B. Amor, "Learning ergonomic control in human-robot symbiotic walking," *IEEE Transactions on Robotics*, vol. 39, no. 1, pp. 327–342, 2023.
- [61] T. R. Clites, M. K. Shepherd, K. A. Ingraham, L. Wontorcik, and E. J. Rouse, "Understanding patient preference in prosthetic ankle stiffness," *Journal of neuroengineering and rehabilitation*, vol. 18, pp. 1–16, 2021.
- [62] W. Bosworth, J. Whitney, S. Kim, and N. Hogan, "Robot locomotion on hard and soft ground: Measuring stability and ground properties in-situ," in *2016 IEEE International Conference on Robotics and Automation (ICRA)*. IEEE, 2016, pp. 3582–3589.
- [63] K. L. Havens, T. Mukherjee, and J. M. Finley, "Analysis of biases in dynamic margins of stability introduced by the use of simplified center of mass estimates during walking and turning," *Gait & Posture*, vol. 59, pp. 162–167, 2018. [Online]. Available: <https://www.sciencedirect.com/science/article/pii/S0966636217309475>
- [64] M. T. Rosenstein, J. J. Collins, and C. J. De Luca, "A practical method for calculating largest lyapunov exponents from small data sets," *Physica D: Nonlinear Phenomena*, vol. 65, no. 1-2, pp. 117–134, 1993.
- [65] P. Terrier and O. Dériaz, "Non-linear dynamics of human locomotion: effects of rhythmic auditory cueing on local dynamic stability," *Frontiers in physiology*, vol. 4, p. 230, 2013.
- [66] S. A. England and K. P. Granata, "The influence of gait speed on local dynamic stability of walking," *Gait & Posture*, vol. 25, no. 2, pp. 172–178, 2007. [Online]. Available: <https://www.sciencedirect.com/science/article/pii/S0966636206000415>
- [67] S. M. Bruijn, J. H. van Dieën, O. G. Meijer, and P. J. Beek, "Statistical precision and sensitivity of measures of dynamic gait stability," *Journal of neuroscience methods*, vol. 178, no. 2, pp. 327–333, 2009.
- [68] F. Takens, "Detecting strange attractors in turbulence," in *Dynamical Systems and Turbulence, Warwick 1980: proceedings of a symposium held at the University of Warwick 1979/80*. Springer, 2006, pp. 366–381.
- [69] H. Kantz and T. Schreiber, *Nonlinear time series analysis*. Cambridge university press, 2004, vol. 7.
- [70] C. Rhodes and M. Morari, "False-nearest-neighbors algorithm and noise-corrupted time series," *Physical Review E*, vol. 55, no. 5, p. 6162, 1997.
- [71] C. Karakasis and P. Artemiadis, "F-VESPA: A kinematic-based algorithm for real-time heel-strike detection during walking," in *2021 IEEE/RSJ International Conference on Intelligent Robots and Systems (IROS)*. IEEE, 2021, pp. 5098–5103.
- [72] C. Karakasis and P. Artemiadis, "Real-time kinematic-based detection of foot-strike during walking," *Journal of Biomechanics*, vol. 129, p. 110849, 2021. [Online]. Available: <https://www.sciencedirect.com/science/article/pii/S0021929021006072>
- [73] A. L. Hof, R. M. van Bockel, T. Schoppen, and K. Postema, "Control of lateral balance in walking: Experimental findings in normal subjects and above-knee amputees," *Gait & Posture*, vol. 25, no. 2, pp. 250–258, 2007. [Online]. Available: <https://www.sciencedirect.com/science/article/pii/S0966636206000580>
- [74] C. Curtze, T. J. Buurke, and C. McCrum, "Notes on the margin of stability," *Journal of Biomechanics*, vol. 166, p. 112045, 2024. [Online]. Available: <https://www.sciencedirect.com/science/article/pii/S0021929024001222>
- [75] J. D. Gibbons and S. Chakraborti, *Nonparametric statistical inference*. CRC press, 2014.
- [76] M. Jacquelin Perry, *Gait analysis: normal and pathological function*, 2010.
- [77] V. S. Shetty, U. H. Lee, K. A. Ingraham, and E. J. Rouse, "A data driven approach for predicting preferred ankle stiffness of a quasi-passive prosthesis," *IEEE Robotics and Automation Letters*, vol. 7, no. 2, pp. 3467–3474, 2022.
- [78] C. Angelidou and P. Artemiadis, "On intuitive control of ankle-foot prostheses: A sensor fusion-based algorithm for real-time prediction of transitions to compliant surfaces," in *2023 IEEE/RSJ International Conference on Intelligent Robots and Systems (IROS)*, 2023, pp. 2122–2127.
- [79] C. Angelidou and P. Artemiadis, "On predicting transitions to compliant surfaces in human gait via neural and kinematic signals," *IEEE Transactions on Neural Systems and Rehabilitation Engineering*, vol. 31, pp. 2214–2223, 2023.
- [80] N. J. Rosenblatt and M. D. Grabiner, "Measures of frontal plane stability during treadmill and overground walking," *Gait & Posture*, vol. 31, no. 3, pp. 380–384, 2010. [Online]. Available: <https://www.sciencedirect.com/science/article/pii/S0966636210000032>
- [81] C. F. Honeycutt, M. Nevisipour, and M. D. Grabiner, "Characteristics and adaptive strategies linked with falls in stroke survivors from analysis of laboratory-induced falls," *Journal of Biomechanics*, vol. 49, no. 14, pp. 3313–3319, 2016. [Online]. Available: <https://www.sciencedirect.com/science/article/pii/S0021929016309113>
- [82] T. M. Owings, M. J. Pavol, and M. D. Grabiner, "Mechanisms of failed recovery following postural perturbations on a motorized treadmill mimic those associated with an actual forward trip," *Clinical Biomechanics*, vol. 16, no. 9, pp. 813–819, 2001. [Online]. Available: <https://www.sciencedirect.com/science/article/pii/S0268003301000778>